9950-1355

FAIRCHILD SPACE

FSC–ESD–217–89–457

SUMMARY OF MISCELLANEOUS HAZARD ENVIRONMENTS FOR HYPOTHETICAL SPACE SHUTTLE AND TITAN IV LAUNCH ABORT ACCIDENTS

M. ECK
M. MUKUNDA

DECEMBER, 1989

FAIRCHILD SPACE • 20301 CENTURY BOULEVARD • GERMANTOWN, MARYLAND 20874

FSC–ESD–217–89–457

SUMMARY OF MISCELLANEOUS HAZARD ENVIRONMENTS FOR HYPOTHETICAL SPACE SHUTTLE AND TITAN IV LAUNCH ABORT ACCIDENTS

FINAL REPORT, JPL CONTRACT 957524

M. ECK
M. MUKUNDA

DECEMBER, 1989

This report was prepared for the Jet Propulsion Laboratory, California Institute of Technology, sponsored by the National Aeronautics and Space Administration.

TABLE OF CONTENTS

LIST OF FIGURES

LIST OF TABLES

INTRODUCTION AND SUMMARY

This report describes the various phases of the analyses performed by Fairchild personnel in support of the Jet Propulsion Laboratory's Galileo Project Office, under Contract No. 95724. The various analyses were aimed at obtaining a more comprehensive understanding and definition of the environments in the vicinity of the RTG during certain STS and Titan IV launch abort accidents. This report addresses a number of issues covering explosion environments and GPHS-RTG responses to those environments. Analyses specific to Centaur in-tank explosions and to solid rocket booster fragmentation are covered in companion reports, FSC-ESD-217-88-435 and FSC-ESD-217-88-426, respectively.

The analyses presented were performed using the PISCES 2D ELK hydrocode. This is a Lagrangian-Eulerian coupled finite-difference code. Eulerian histories of blast flow parameters were calculated as a function of time and distance and the response of structures to the blast flow were analyzed by coupling the Eulerian flow field to Lagrangian structures.

The material in this report involves the subtasks summarized below and discussed in detail in the subsequent chapters.

I. BLAST LOADING AND CYLINDRICAL PRESSURE DISTRIBUTION

A detailed analysis was made to calculate the pressure distribution around a rigid cylinder when subjected to a blast flow field producing a peak overpressure of 1070 psi. The loading around the periphery of the cylinder was extracted as a function of the distance of the standing shock wave upstream from the stagnation point.

II. SHOCK TUBE TEST ENVIRONMENTS

A number of explosively driven shock tube tests were conducted by the personnel at Sandia National Laboratory. Segments of the RTG converter and GPHS modules were placed in a 1.89 foot diameter shock tube and exposed to peak static overpressures ranging from 495 psi to 2000 psi by exploding varying amounts of the condensed explosive C-4. FSC personnel performed a series of parametric analyses to simulate the blast flow environment in the shock

tube in order to evaluate and define the actual loading on the test article. The hydrocode results were calibrated against experimentally observed overpressure traces. The analyses confirmed that the damaging effect of the C-4 high-density debris was much more severe than would be experienced by an RTG subjected to a blast wave created by the detonation of liquid oxygen and liquid hydrogen.

III. SHIELD DESIGN STUDIES

Personnel at JPL proposed two different kinds of shields as possible protection for the RTG against blast and fragment environments. FSC personnel performed a series of calculations for various blast environments and shield designs. It was evident from these analyses that for any reasonable shield mass the shield itself would destroy the integrity of the aeroshell which is the main re-entry protection component of the RTG. This was unacceptable and the approach was abandoned by JPL.

IV. STS 51L EXTERNAL TANK BREAKUP

After the Challenger (STS 51L) accident in January, 1986, FSC personnel were tasked to explain the large expanding "combustion cloud" associated with the Challenger breakup and observed in the photographic records. The cryogens were modelled using the Euler processor. Appropriate equations of state were developed for the liquid hydrogen and oxygen. Plots of material location were made as a function of time and were compared with the optical data reduction performed by RDA personnel [1]. Although very good agreement was obtained with initial clad geometry the analysis showed that the observed cryogen cloud could not be explained solely as a result of the isentropic expansion of the cryogens stored in the external tank. It was concluded that energy added to the hydrogen by burning in air was necessary to duplicate the observed cloud geometry.

V. ET SPILL CALCULATIONS

JPL personnel proposed several accident scenarios involving the spillage of the STS-ET-stored propellants on the launch pad. FSC personnel evaluated each of these

environments and the analyses showed that the expansion of the cryogens during the fall from gantry heights tends to inhibit the mixing of the cryogens on the ground surface.

VI. ORBITER RESPONSE TO SPILL BLAST

JPL proposed an accident scenario wherein a pool of cryogens, one foot in depth, accumulated on the mobile launch platform and detonated causing a blast wave to interact with the orbiter. FSC personnel modelled the two phase cryogen mixture and allowed it to detonate using the well known Taylor blast wave similarity solution. The shock wave thus generated was tracked for a distance of 10 meters and allowed to interact with the orbiter rigid structures, e.g. the main engines, IUS and probe, and the cargo bay doors. The calculations were made in two different modes, one in which the axis of the bay was parallel to the flow and the other in which the axis was normal to the flow field. Both calculations showed that there was a build up of pressure outside the bay doors resulting in the bay doors collapsing inwards at velocities between 60 and 100 m/s.

VII. RESPONSE OF RTG TO IMPACT OF FORWARD CLOSURE TITAN FRAGMENT

The response of an RTG to the impact of fragments from failed SRB's became a major concern after the Challenger accident. FSC personnel set up a detailed model to investigate the effect of end-on impacts of fragments due to failure of the Titan forward SRM closure. This support effort was conducted to define the environmental specifications for the Titan IV Data Book. The translational symmetry model included the RTG end cover, end insulation, the titanium spider and the (one-half) inch 3D graphite block at the end of the stack. The analysis showed that, due to a lack of inertial restraint in the direction orthogonal to the impact plane, large distortions of the fuel capsules resulted. A number of parametric runs was made to span the probable impact velocity, fragment, and thickness ranges.

Each of the above sections is discussed in detail in the following chapters.

I. BLAST LOADING AND CYLINDRICAL PRESSURE DISTRIBUTION

The material presented in this chapter describes the analysis performed by FSC personnel to simulate the blast flow around a rigid body in a shock tube environment. The shock tube environment of interest was a 1070 psi static overpressure air blast interacting with a rigid cylinder. The analysis was conducted in two phases.

A. Generation of the Flow Field Environment, and
B. Interaction of the Flow Field with an 8.50 Inch Diameter Cylinder Inside a 1.89 foot diameter shock tube.

Each of these phases will be discussed in turn.

A. Generation of the Flow Field

A series of explosively driven shock tube tests was conducted by the Sandia National Laboratory in Albuquerque, NM [2]. An explosive mass of 110 lbs of C-4 placed at the mouth of a 1.89 ft diameter shock tube was observed to generate a static overpressure of 1070 psi at a test station 63.9 feet down the length of the shock tube. It was suggested that a reasonable simulation could be obtained if it were assumed that 20 percent of the 110 lbs of C-4 was uniformly distributed across the cross sectional area of a 1.89 foot diameter tube. The one-dimensional Lagrangian continuum-mechanics-code PISCES 1DL was used to set up the problem. The resulting thickness of the column of C-4 to account for the mass of C-4 entering the tube is given by:

$$t = \frac{M_{C4}}{\rho_{C4}} \cdot \frac{1}{\pi d^2 / 4} \tag{1}$$

where:

M_{C4} = (.20) (110) lbs = mass of C-4
ρ_{C4} = 1.601 g/cm^3 = density of C-4
d = 1.89 ft = diameter of tube
t = 2.3924 cm

PISCES 1DL is a one-dimensional Lagrangian continuum-mechanics-code similar to PUFF, WONDY, etc. The calculation was set up in plane symmetry, the "left" surface of the explosive was a rigid wall, the right surface free to expand against gamma law air at ambient pressure. The explosive was "volume burn" initialized, justifiable on the basis of test station location distance from the explosive (63.9 feet) compared to explosive thickness (2.3926 cm). A JWL equation of state [3] was used for the explosive given by:

$$P = A\left[1 - \frac{\omega\eta}{R_1}\right]\exp\left[\frac{-R_1}{\eta}\right] + B\left[1 - \frac{\omega\eta}{R_2}\right]\exp\left[\frac{-R_2}{\eta}\right] + \omega\eta\rho_0 e \qquad (2)$$

where:

$A = 6.9077$
$B = 0.295$
$R_1 = 4.5$
$R_2 = 1.4$
$\omega = 0.24$
η = 1/v, where v is the relative volume

Test data were available for the static pressure time history at two stations located at 53.6 feet (1633.7 cm) and at 59.6 feet (1816 cm) from the explosive. The static pressure was monitored at these two locations in the calculations and is plotted along with the observed profiles in Figures 1 and 2. Examination of these two figures indicates a reasonably good fit with the experimental results.

A 1DL run was then performed with the above environmental conditions along with a rigid right boundary at station 64.25 ft (1958.6 cm). The purpose of this run was to establish a left boundary location for a subsequent 2D run. A station at 1250 cm (41 feet) was considered appropriate to start a two dimensional calculation. A final 1DL run was made to generate the flow parameters at the 1250 cm station, and Eulerian time histories of static pressure, velocity, density and specific internal energy were extracted.

B. Blast Loading of Cylinder

A two-dimensional model was set up using the Euler processor in the PISCES 2D ELK code. The wall of the shock tube was simulated by defining no flow i.e., reflecting boundary conditions. The grid consisted of an 87 x 27 network with a mesh size of 1 cm x 5 cm in the region of interest. An 8.50 inch cylinder was then modelled using the rigid body processor

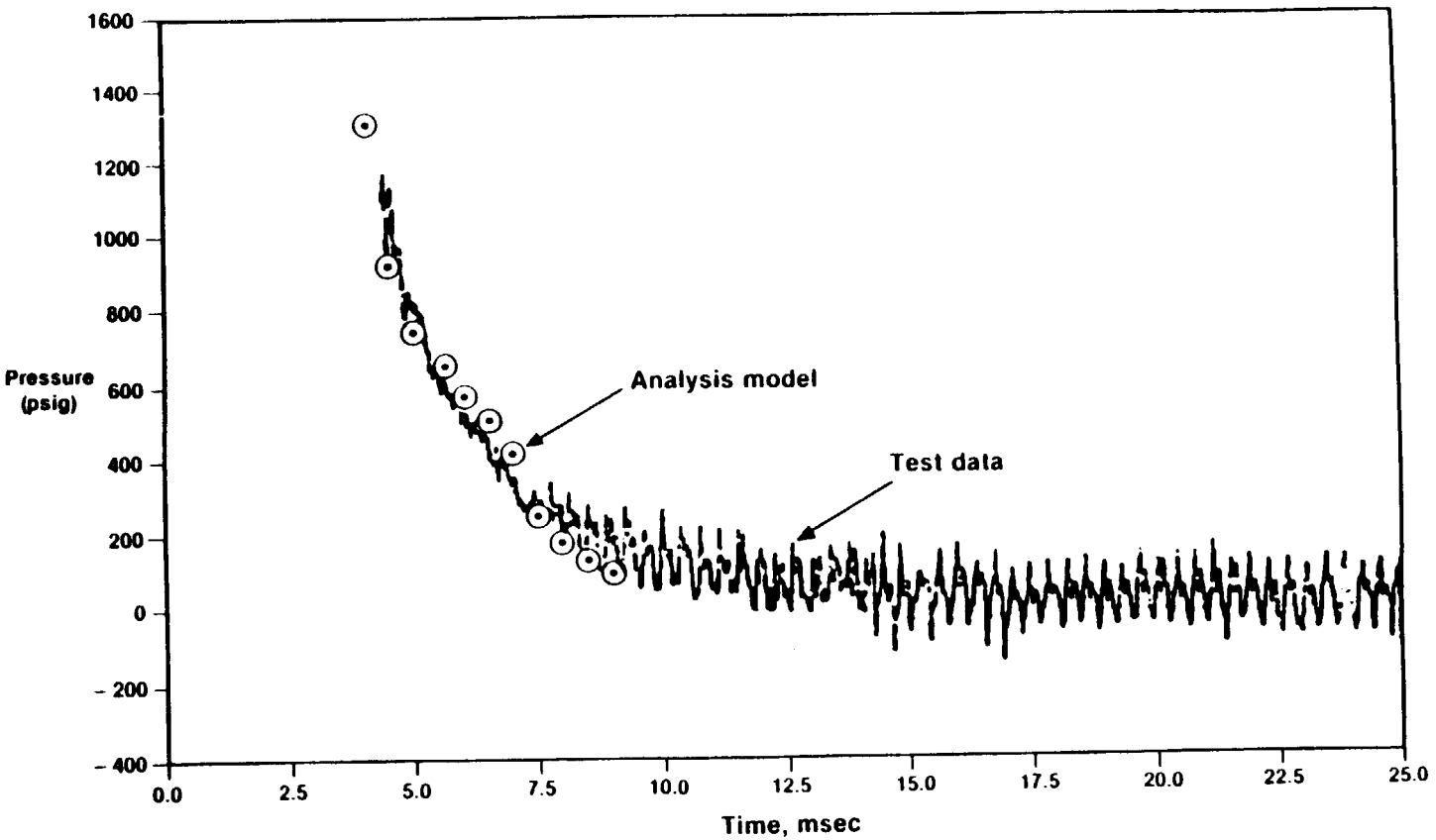

Figure 1. Pressure Time History Measured in the Shock Tube Sidewall 10.3 ft Upstream from Test Cylinder Location

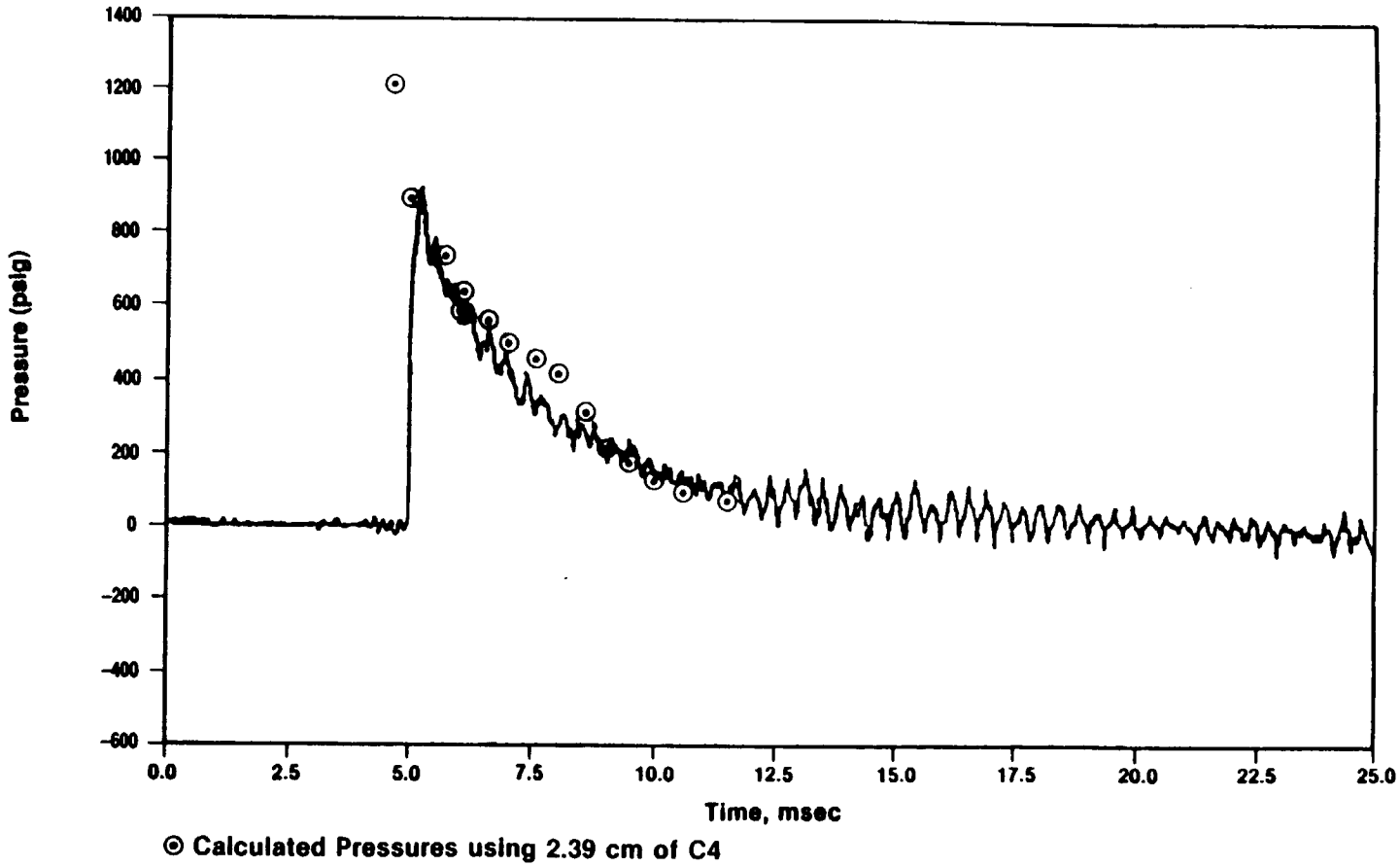

Figure 2. Pressure Time History Measured in the Shock Tube Sidewall 4.28 ft Upstream from the Test Cylinder Location

contained in the PISCES 2D ELK code. The cylinder was given a mass of 10 kg to minimize its movement during the period of interest. Figure 3 depicts the model used for the analysis.

The PISCES code has a boundary flow capability referred to as EXFLOW. This option allows "feeding" blast wave parameters, (e.g. density, velocity and internal energy) to the Euler processor. The EXFLOW parameters stored in the previous 1D PISCES run were fed into the left edge of the Euler grid and the resulting blast field was allowed to flow over the cylinder. Figures 4, 5, and 6 indicate the typical velocity vectors and pressure contours around the cylinder at 560, 640, and 680 μs respectively after feeding the 2D Euler.

Eulerian time histories of static pressure and dynamic pressure around the cylinder were extracted and the data were analyzed to obtain the pressure distributions around the body for different locations of the standing shock front upstream of the cylinder. These results were transmitted to JPL in order to facilitate the generation of an update to the blast loading model currently in use.

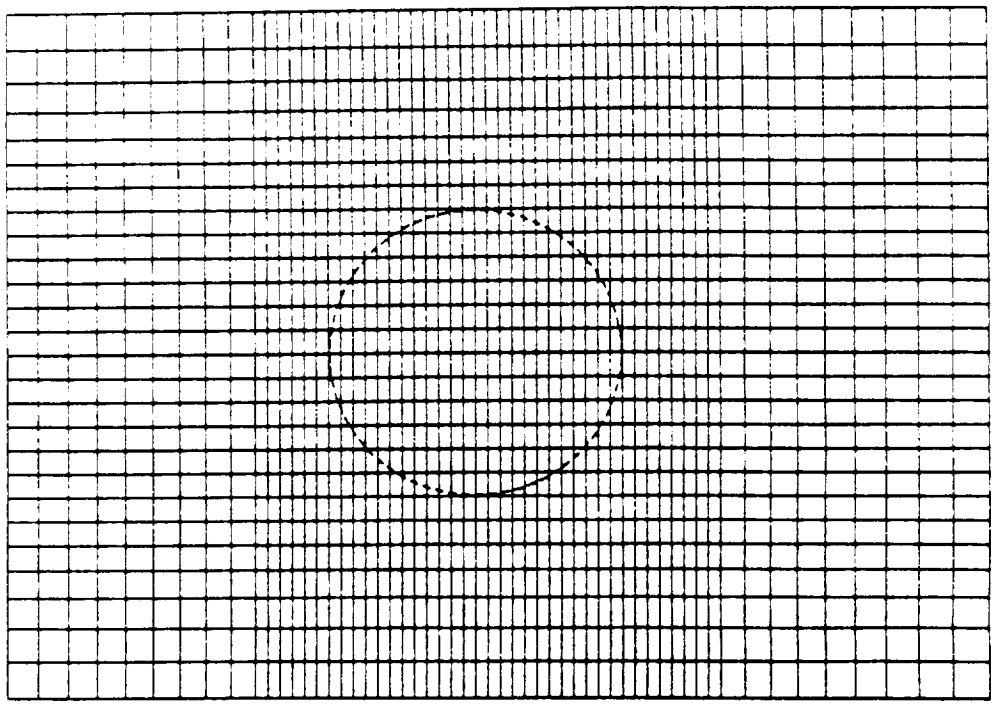

Figure 3. Model of EULER Grid and Cylinder

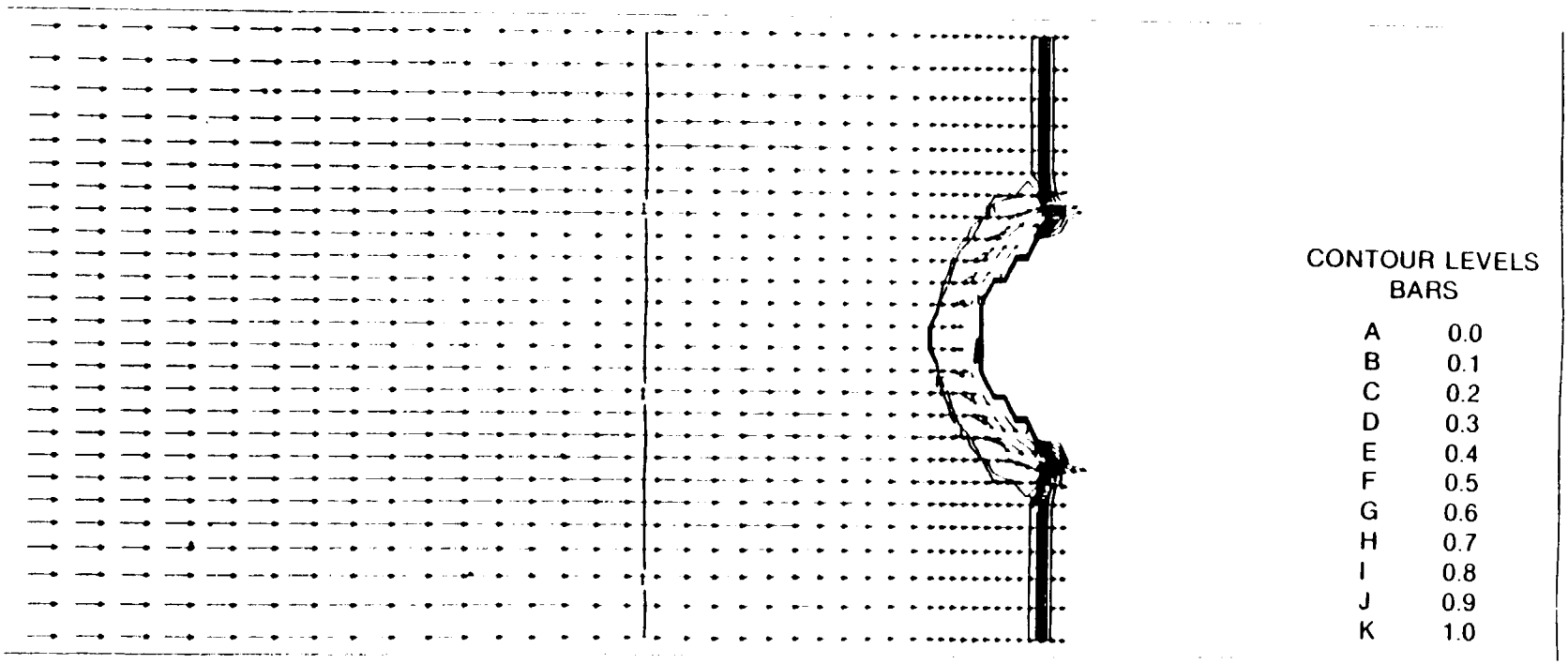

Figure 4. Pressure Contours in Shock Tube at 560 μSEC

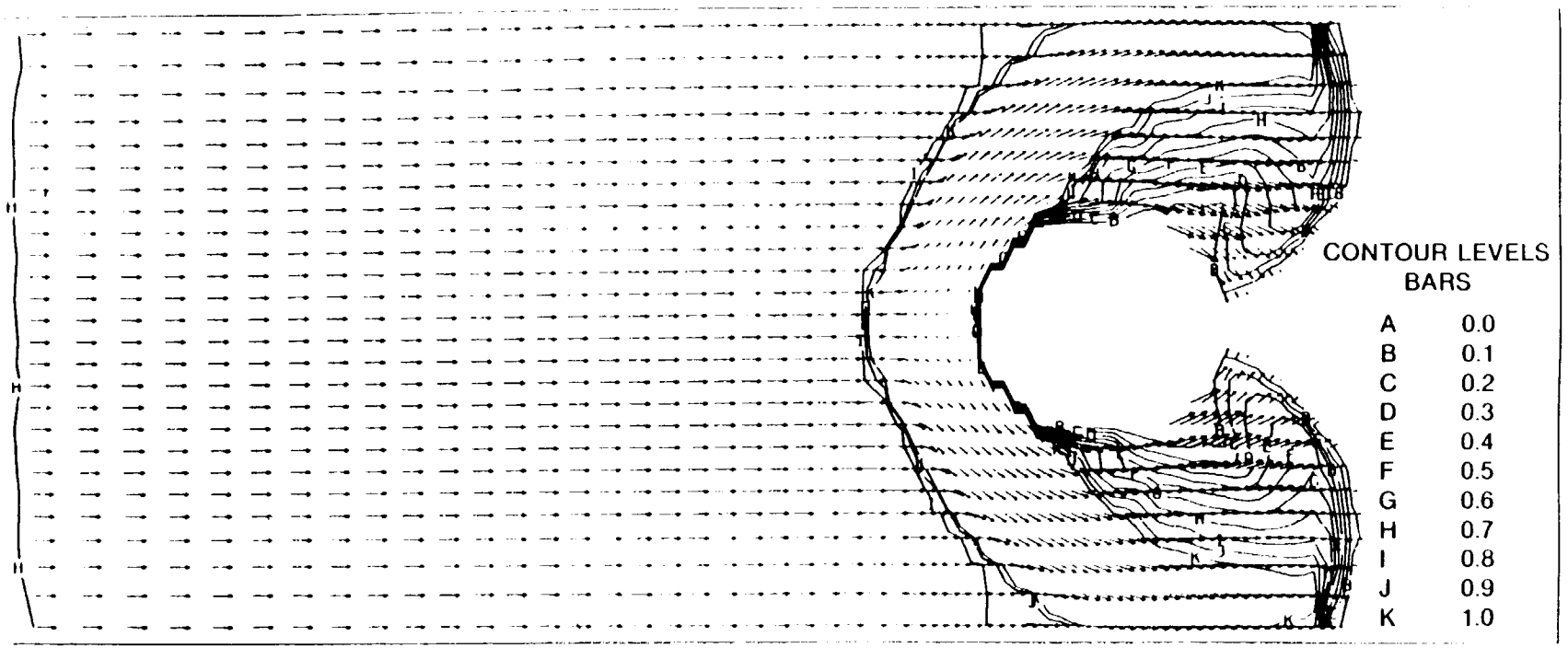

Figure 5. Pressure Contours in Shock Tube at 640 μ SEC

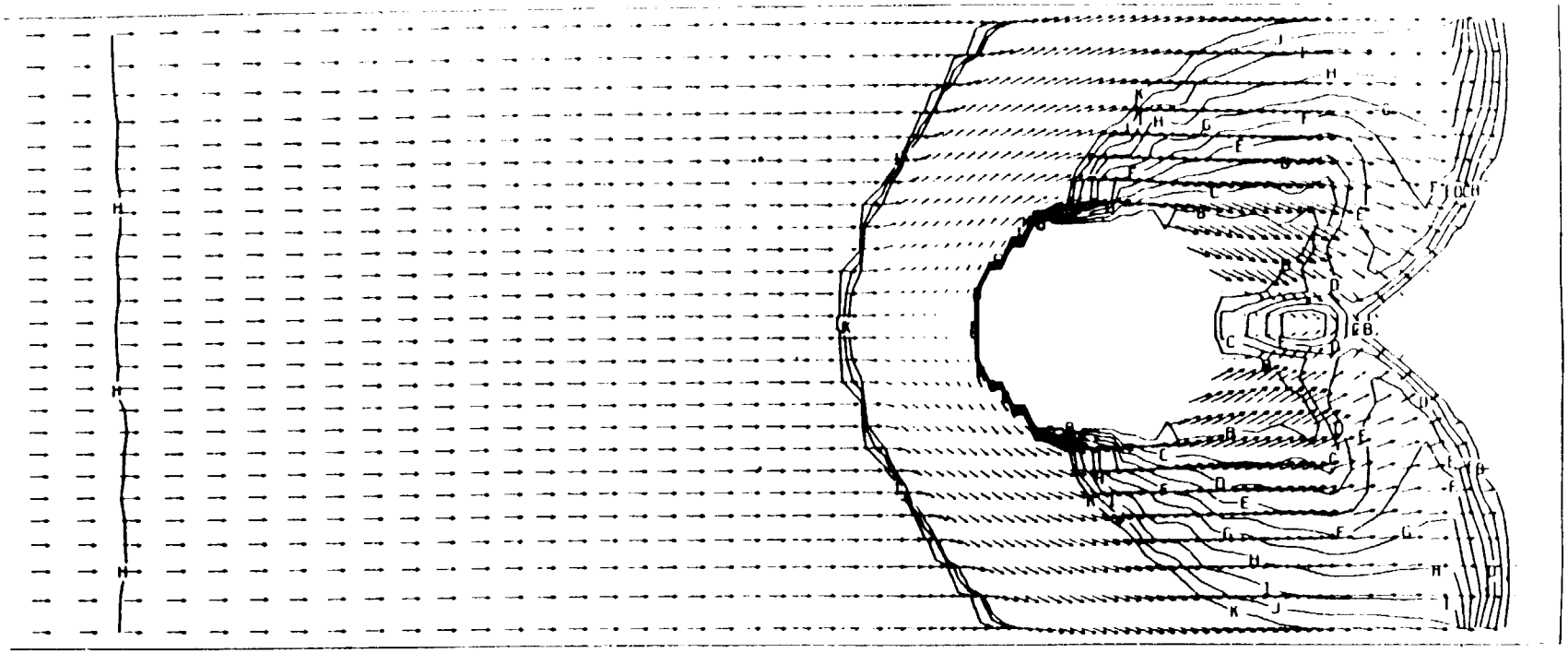

CONTOUR LEVELS
BARS

A	0.0
B	0.1
C	0.2
D	0.3
E	0.4
F	0.5
G	0.6
H	0.7
I	0.8
J	0.9
K	1.0

Figure 6. Pressure Contours in Shock Tube at 680 μSEC

II. SHOCK TUBE TEST ENVIRONMENTS

The analyses performed by FSC personnel in support of the shock tube experiments conducted for the U.S. Department of Energy at Sandia National Laboratories are described in Chapter II. This Chapter is divided as follows:

A. The evaluation of the shock tube test environments and,
B. Simulation and analysis of the shock tube test environments.

Both of these areas will be discussed in detail.

A. Evaluation of the Shock Tube Test Environment

A series of explosively driven shock tube tests was conducted to establish the response of the GPHS to potential STS abort environments. These tests were conducted on Coyote Range of the Sandia National Laboratory at Albuquerque, N.M. by Sandia personnel. The data acquisition and reduction methods used for these tests have been previously published [2]. These methods were used to estimate the peak dynamic pressures felt by the test article in the shock tube tests.

The analysis performed to estimate the peak dynamic pressures experienced by the test article from the time of arrival data provided by Sandia personnel are described in this section. Three explosion overpressure tests were analyzed. In BMT-3, 110 lbs of C-4 was detonated to yield an overpressure of 1070 psi at the location of the test article. In CST-4, 256 lbs of C-4 was detonated to yield an overpressure of 1750 psi at the location of the test article. In CST-8, 27.5 lbs of C-4 was detonated to yield an overpressure of 429 psi at the location of the test article.

Four pressure gauges mounted in the shock tube wall upstream from the test station sensed the arrival time of the shock front. Table I defines the parameters used in the calculation where Ps, Q and U are dimensionless variables defined in terms of the local atmospheric pressure Po and sound speed c_o. Tables II, III, and IV indicate the results of the

Table I. Parameter Definition

Parameter	Symbol	Equation
Peak static overpressure	$\overline{P_s}$	P_s/P_o
Peak dynamic pressure	$\overline{Q}$	Q/P_o
Shock velocity	$\overline{U}$	U/a_o
where: $P_o = 12.1$ psi		
$a_o = 1115$ ft/sec		

The results of these calculations are presented in Table II, III, and IV.

S-201.00

Table II. Environmental Conditions in CST8

Positions (1) (x) ft	Shock Arrival Time (t) ms	U(2) ft/sec	Ps(2) psi	Q psi
31.35	2.91	8783	862	--
38.35	3.73	8195	748	--
52.35	5.56	7228	579	--
59.34	6.55	6826	515	--
Test 63.73	7.21(3)	6595	480	1200

(1) First four rows represent pressure transducer locations. The RTG is located at 63.73 feet.

(2) Calculated from time of arrival curve fit
$t = 0.879574E\text{-}1 + (.77285E\text{-}1)\,X + (.583239E\text{-}3)X^2$

(3) Inferred from four time of arrival measurements using same curve fit.

S-201 01

Table III. Environmental Conditions in BMT-3

Positions (1) (x) ft	Shock Arrival Time (t) ms	U(2) ft/sec	Ps(2) psi	Q psi
35.589	2.572	11264	1426	--
47.609	3.674	10591	1259	--
53.609	4.245	10284	1186	--
59.619	4.841	9994	1120	--
Test 64.3	5.314(3)	9778	1071	4100

(1) First four rows represent pressure transducer locations. The RTG is located at 64.3 feet.

(2) Calculated from time of arrival curve fit
$t = -0.29082187 + 7.2065798E\text{-}2X + 2.347739E\text{-}4X^2$

(3) Inferred from four time of arrival measurements using same curve fit.

S-201 02

Table IV. Environmental Conditions in CST4

Positions (1) (x) ft	Shock Arrival Time (t) ms	U(2) ft/sec	Ps(2) psi	Q psi
30.959	1.829	13802	2150	--
42.969	2.739	13199	1964	--
48.975	3.159	12918	1880	--
54.990	3.661	12647	1802	--
Test 59.302	3.996(3)	12460	1748	7260

(1) First four rows represent pressure transducer locations. The RTG is located at 59.3 feet.

(2) Calculated from time of arrival curve fit
$t = -0.27924 + 6.3928E\text{-}1X + .13766E\text{-}3X^2$

(3) Inferred from four time of arrival measurements using same curve fit.

S-201 03

calculations for peak static pressure, peak dynamic pressure experienced by the test article in the various shock tube tests performed at Sandia National Laboratories.

The velocity of the shock front at the test station was calculated using a curve fit to the time of arrival data at the upstream pressure gauges. The peak overpressure at the test station was calculated using the equation governing normal shocks in a perfect gas [4].

$$\frac{P_y}{P_x} = \frac{2\gamma}{\gamma+1} \cdot M_x^2 - \left[\frac{\gamma-1}{\gamma+1}\right] \tag{3}$$

$$P_y - P_x = P_x \frac{[2\gamma (M_x^2 - 1)]}{\gamma+1} \tag{4}$$

The dynamic pressure at the test station was then estimated using the shock front parameters for incident air blast waves compiled by Baker [5]. The curves for these parameters are presented in Figure 7 and the symbols are explained in Table I.

B. Simulation and Analysis of the Shock Tube Test Environments

A number of investigators had observed that shock tube tests may not accurately simulate the real environments felt by the RTG in the case of an abort. FSC personnel performed analysis to evaluate the effect of the following constraints imposed by the shock tube environment:

1. The effect of shock tube walls on static and dynamic pressure and impulses and,

2. The effect of high explosive reaction products on the blast flow field.

Both of these factors will be discussed in detail.

1. The Effect of Shock Tube Walls. This analysis was performed for the shock tube test CST-2 which was determined to have an overpressure of 1070 psi at the test article location 63.9 feet down the shock tube. The flow field environment was generated as described in the

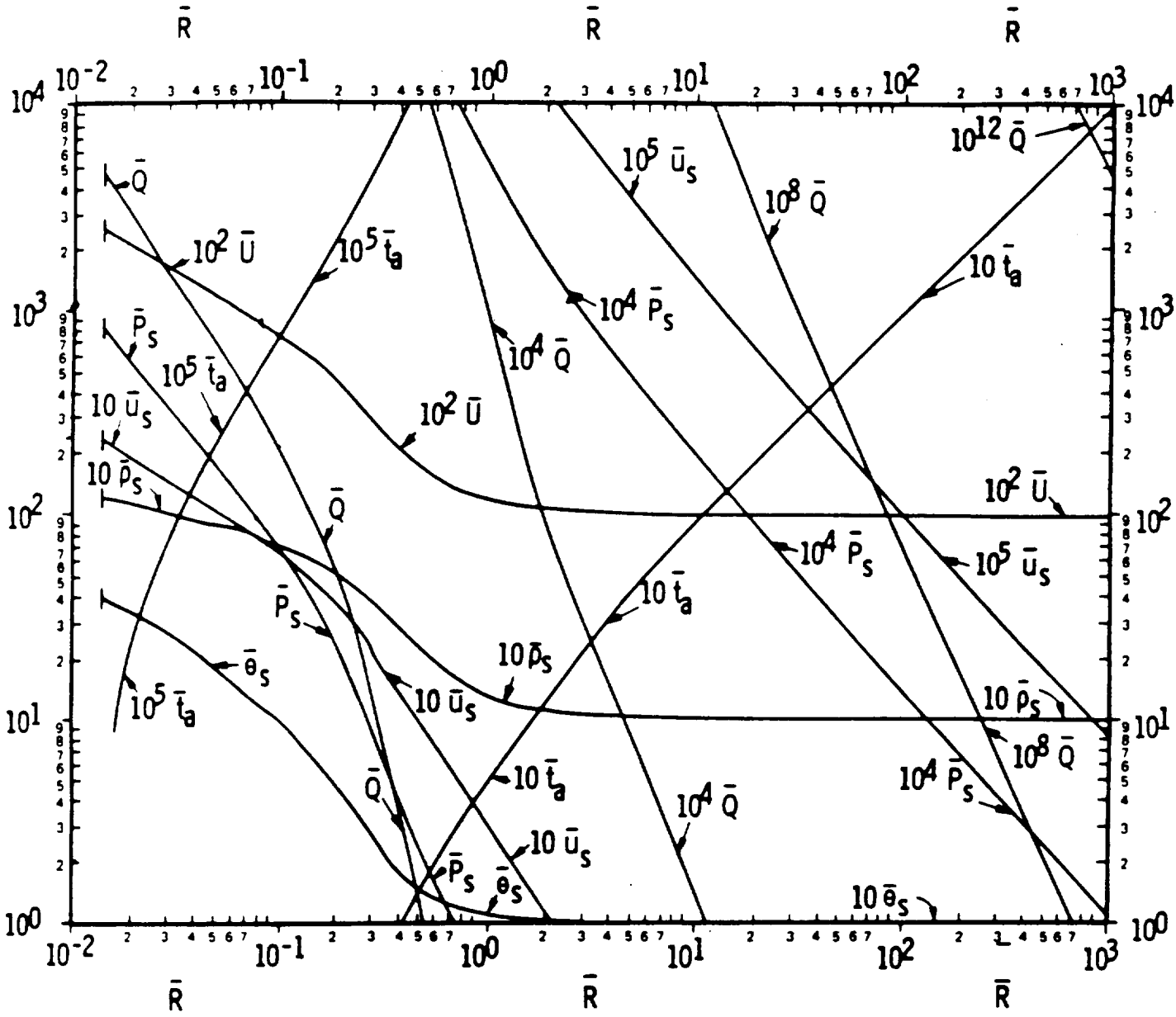

Figure 7. Compiled Shock-Front Parameters for Incident Air Blast Waves [5]

the previous section. The shock tube and the RTG housing were modelled in translational symmetry.

The air in the shock tube was modeled using the Euler processor and the walls of the tube were simulated by imposing the boundary constraint of a no-flow wall. The air was assumed to be at ambient pressure and to obey the gamma gas law. The RTG housing was modelled using the Lagrangian processor embedded in the PISCES 2D ELK code. The housing was modelled as a 9.53 inch diameter cylinder with a wall thickness of 0.06 inches.

The calculations performed with a wall boundary constraint are indicated by the data set name CYLTUBW and those with a free flow boundary condition are indicated by the data set name CYLTUBF. Figures 8 and 9 depict the pressure contours and the velocity vectors of the flow field interacting with the housing for constrained (CYLTUBW) and free flow boundaries (CYLTUBF).

Figures 10 and 11 indicate the particle velocity of the air at the housing for CYLTUBW and CYLTUBF. Figures 12 and 13 exhibit the dynamic impulse experienced by the housing for the two scenarios.

Examination of these figures indicates that the effect of the flow constrain caused by the shock tube wall is negligible.

2. The Effect of the HE Products on the Blast Flow Field. The environments for Sandia National Laboratories CST-4 and BMT-3 was simulated analytically. In this test, 256 lbs and 110 lbs C-4 were detonated at the open end of the shock tube. As described earlier, the flow field was generated first in plane symmetry and then fed into the 2D Euler model of the shock tube. The resulting time history of dynamic pressure at the housing location was plotted in Figure 14 for static overpressures of 1070 psi and 1800 psi, (tests BMT-3 and CST-4).

Unfortunately, no dynamic pressure measurements were performed to provide a calibration of the analyses. Examination of the profiles indicates that the peak dynamic pressure resulting from a pure air shock is less than that due to the arrival of the much heavier (density = 1.6 gm/cm) particulate debris carried along by the expanding high explosive (HE).

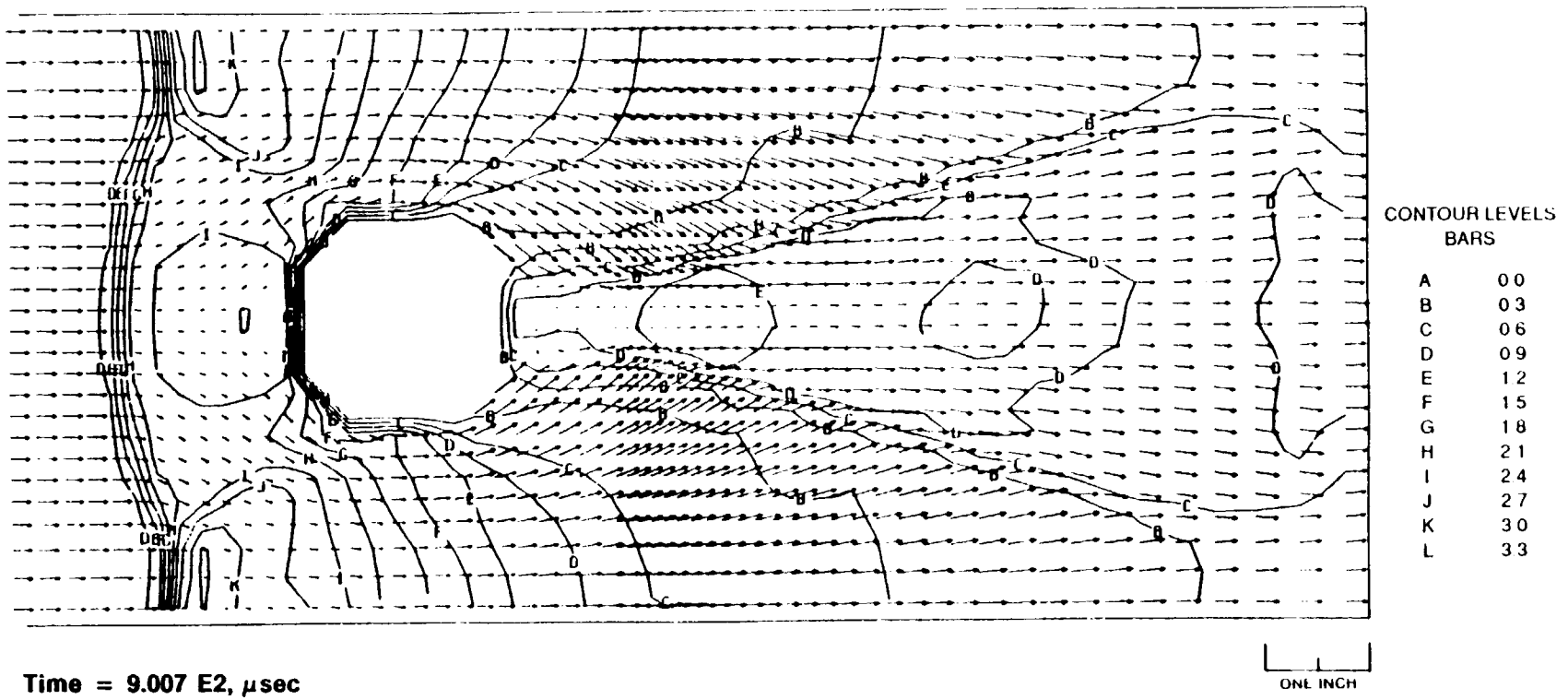

Figure 8. Pressure Contours in Shock Tube with Wall Boundary, CYLTUBW

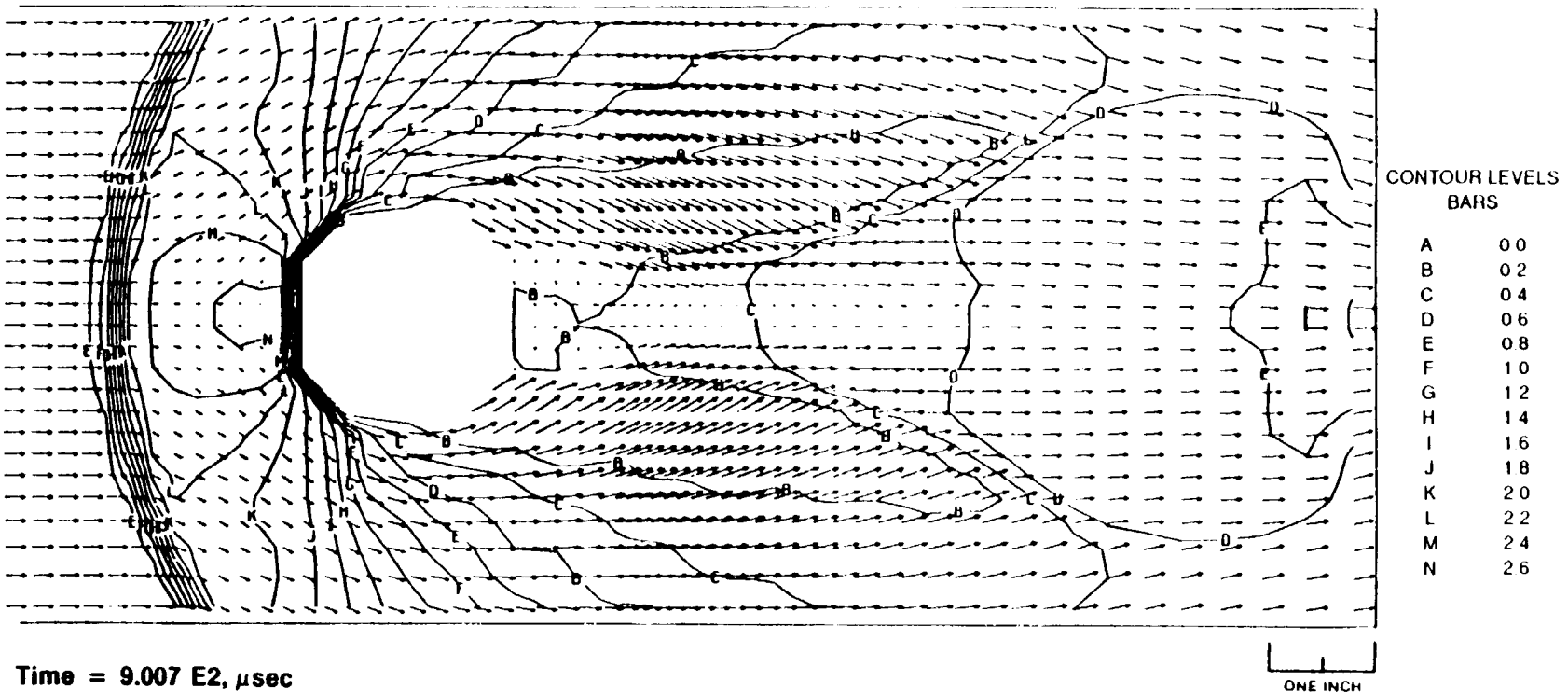

Figure 9. Pressure Contours in Shock Tube with Flow Boundary, CYLTUBF

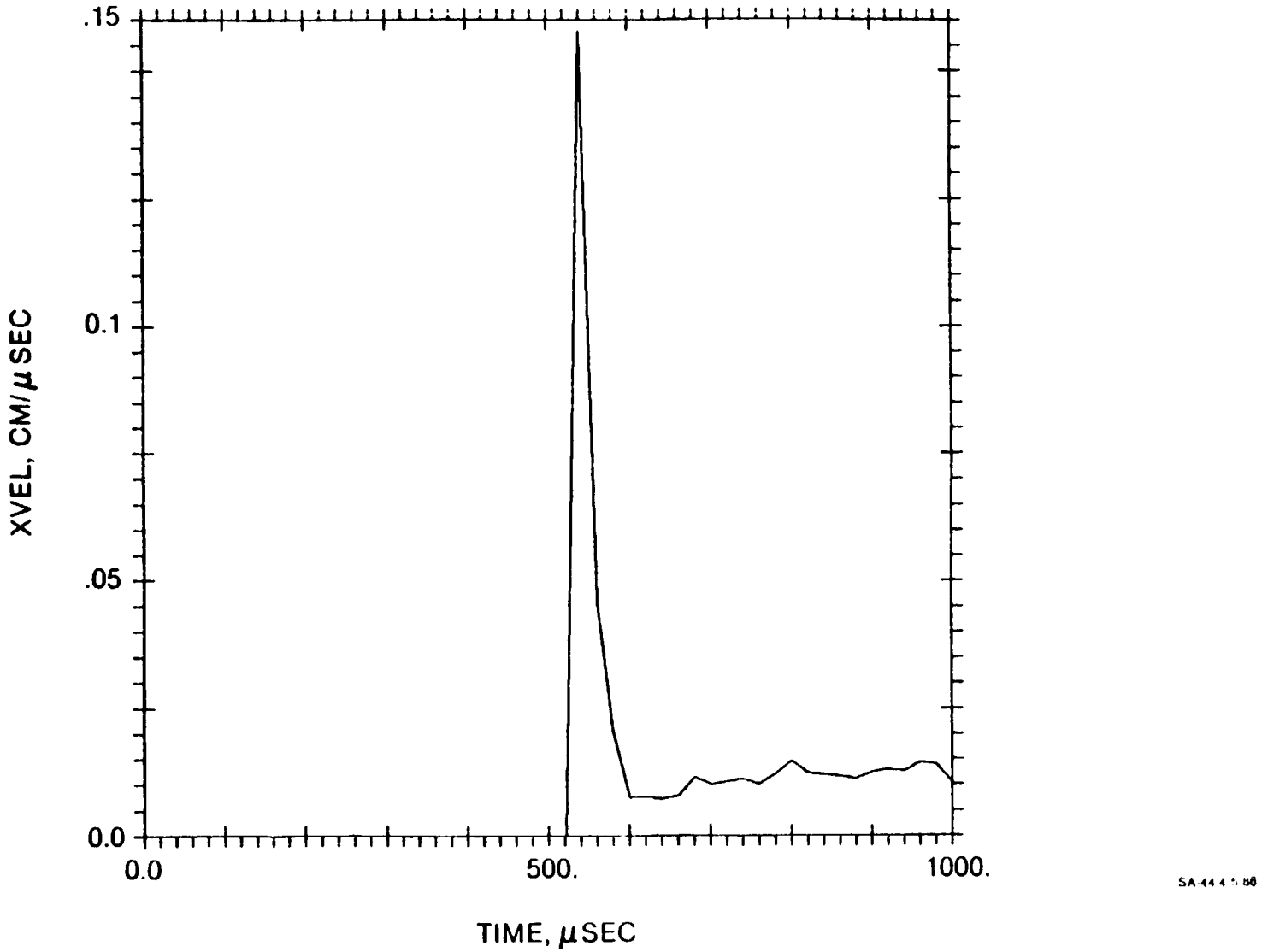

Figure 10. Time History of Particle Velocity at Simulated RTG Housing with Shock Tube Wall Boundary (1070 PSI CYLTUBW)

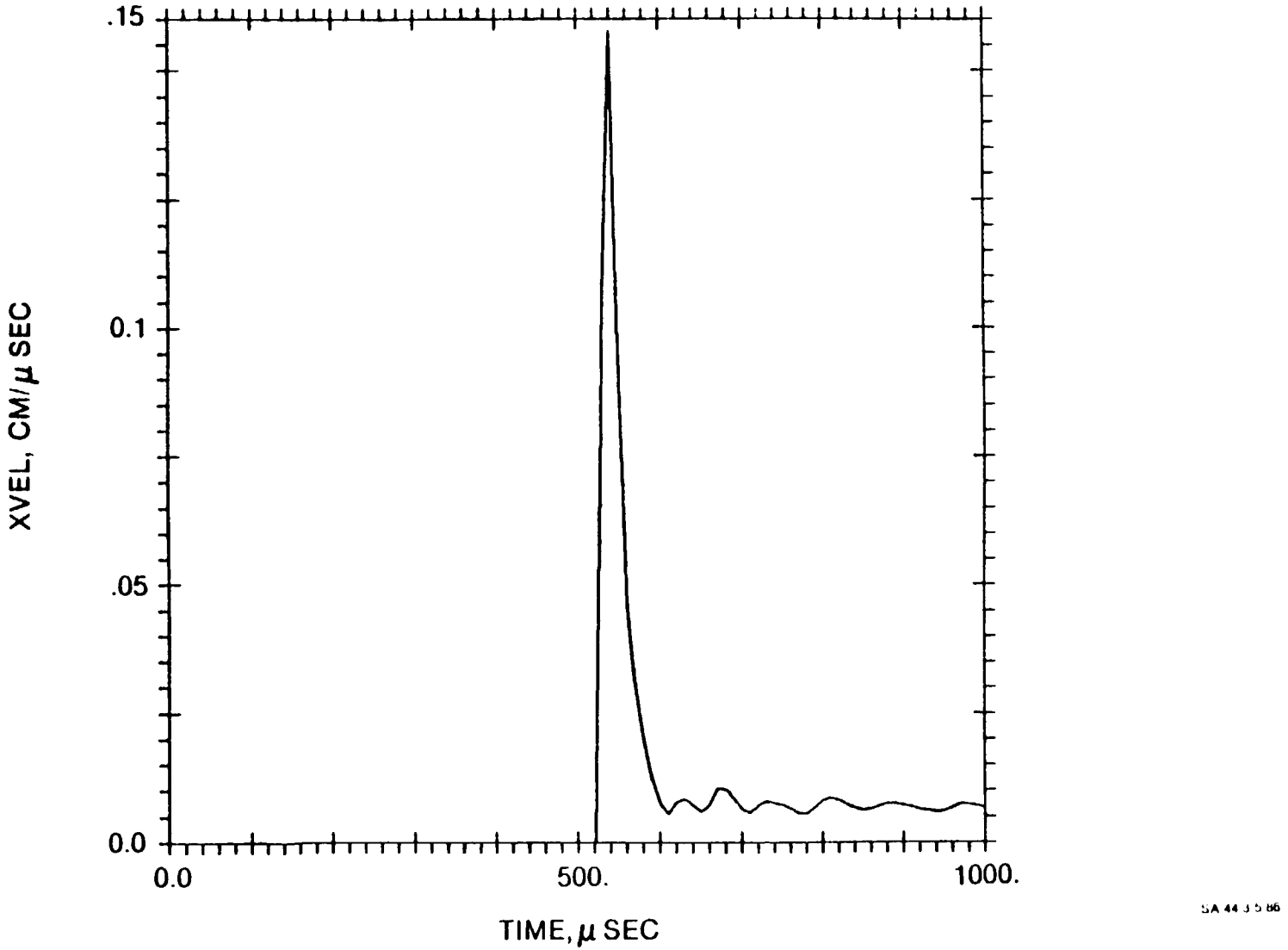

Figure 11. Time History of Particle Velocity at Simulated RTG Housing with Flow Boundary (1070 PSI CYLTUBF)

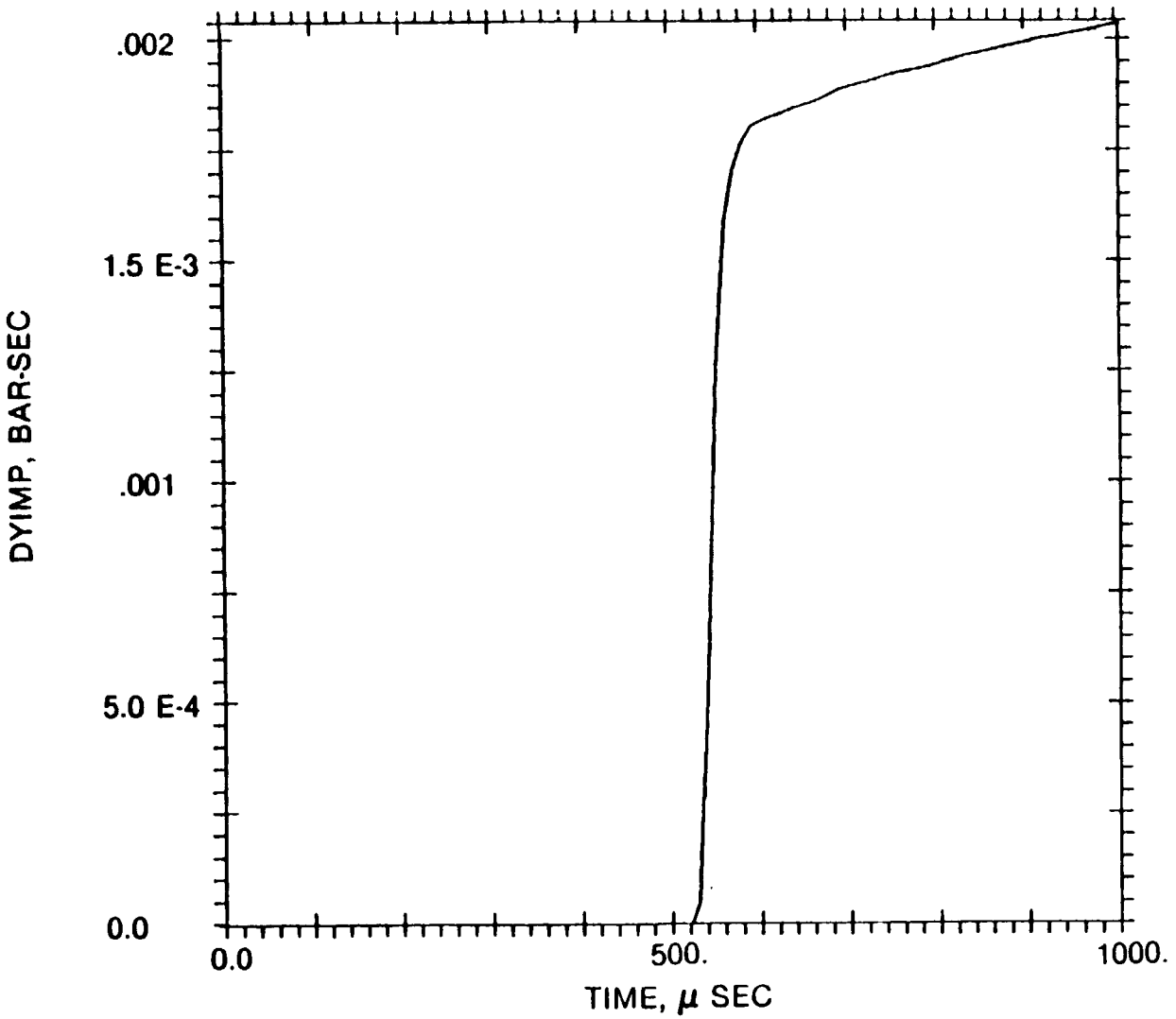

Figure 12. Time History of Dynamic Impulse at RTG Housing with Shock Tube Boundary (1070 PSI CYLTUBW)

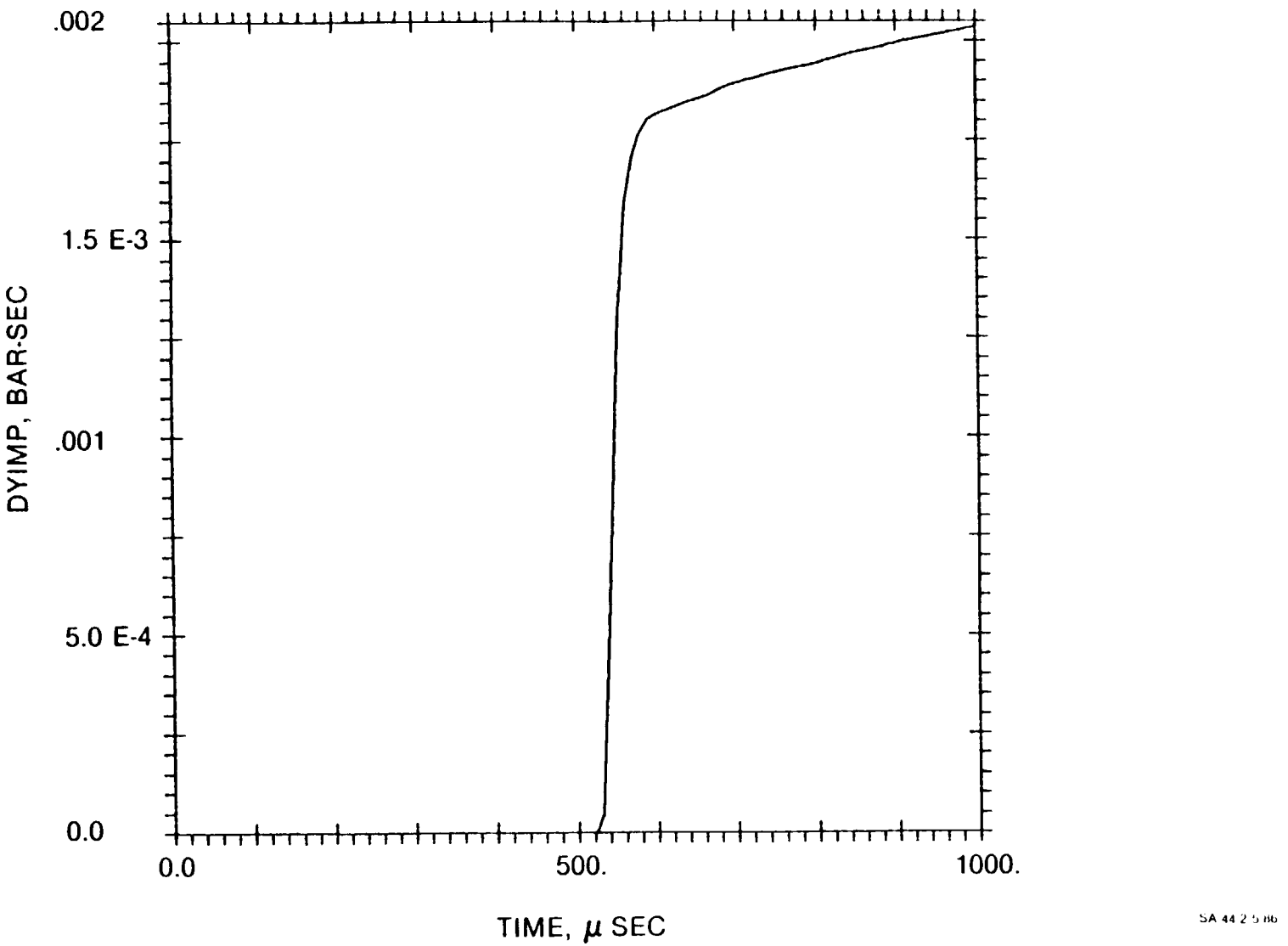

Figure 13. Time History of Dynamic Impulse at RTG Housing with Flow Boundary (1070 PSI CYLTUBF)

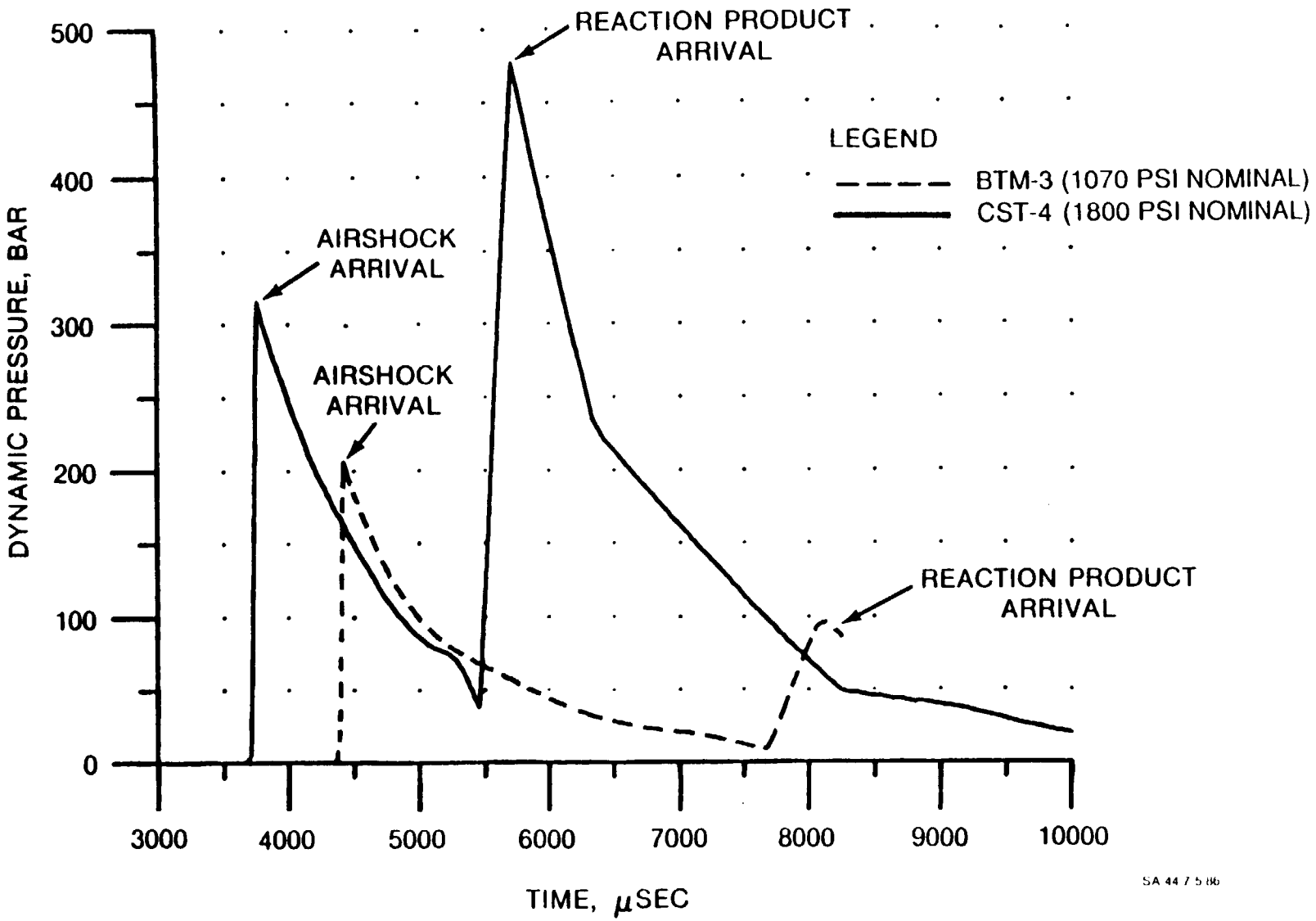

Figure 14. Time History of Dynamic Pressure Predicted for Two Shock Tube Tests

As the static overpressure increases, the increase in the peak dynamic pressure due to the HE products is magnified and the time lag between the pure air shock arrival and the HE products arrival decreases significantly.

Since dynamic pressure can be considered to be kinetic energy density, it represents a capacity to do work and damage. Thus the HE products increase the severity of GPHS module response to the blast flow field.

III. SHIELD DESIGN SUPPORT

This section describes the details of the analyses performed by Fairchild personnel in order to evaluate the protection offered by a shield to the GPHS modules when they were subjected to various explosion environments.

A. Explosion Environments

The explosion environments of interest were those generating the following peak static overpressure at the shield: (a) 495 psi; (b) 1070 psi; (c) 1760 psi; (d) 2000 psi. Each of these environments was generated by first setting up a 1D plane symmetry model with an appropriate column of explosive C-4 expanding into air at ambient pressures. The details of the generation of the 1070 psi environment have been described in Sections I and II. Personnel at the Sandia National Laboratory [6] ran a series of incrementally higher explosion overpressure tests in which a GPHS module surrounded by an RTG housing simulant was exposed to blast waves to simulate launch pad accidents. In particular, in test CST-6-RTG-2, 300 lbs of C-4 was detonated to yield an overpressure of 1962 psi at the test station, and in test CST-8-RTG-4, a charge of 27 lbs of C-4 was detonated to yield an overpressure of 429 psi.

The blast flow parameters, namely the density, velocity and specific internal energy were subsequently fed into a 2D-Euler grid containing the shield described in the following section.

B. Shield Design

Two different kinds of shields were proposed by JPL and analyzed using the PISCES two-dimensional hydrocode in translational symmetry. The details of the two designs are given below.

1. Buffer Shield Approach

The buffer shield consists of a 0.875 inch thick titanium can of radius 8.1 inches with eight crush blocks of FWPF distributed around the circumference. The crush blocks were approximately 3.7 inches thick. The model of the GPHS module surrounded by its housing

and the buffered shield is shown in Figure 15. The material equations of state for the FWPF, POCO, iridium and fuel in the module have been described in earlier reports [7]. The equation of state for the titanium can was obtained from a report by Bakken and Anderson [8]. The titanium has a density of 4.42 gm/cm^3 with a bulk modulus of 994 kb, shear modulus of 415 kb and a yield strength of 9 kb.

The GPHS module surrounded by its housing and the shield were subjected to an explosive blast flow field having peak values of static overpressure of 1070 psi, 1760 psi and 2000 psi.

Figure 16 exhibits typical results of the calculation. It depicts the shield and its contents being exposed to peak static overpressures of 1070 psi, 1760 psi and 2000 psi, respectively. Examination of the figures indicates a definite failure of the titanium can in a flow field of 2000 psi, neither does the shield survive the JPL demand loading profile for the 1760 psi test. Even at lower blast wave intensities, the shield displays a high degree of ellipticity well before any initiation of damage to the GPHS.

The calculations showed that a pressure vessel concept cannot adequately deal with the specified environments. A decision was made to abandon this buffer shield approach, and no further calculations were performed on this model.

2. Honeycomb Shield Approach

The honeycomb shield design developed by JPL consisted of a 4 inch thick aluminum honeycomb material sandwiched between a 0.2 inch thick steel outer skin and a 0.1 thick aluminum inner skin.

A p-α hydrodynamic compaction equation of state was developed for the honeycomb material. Calculations were made for densities of 10 lbs/ft^3 and 22 lbs/ft^3 for the honeycomb material. A p-α model requires a distention ratio

$$\alpha = \frac{\rho}{\rho_s} \tag{5}$$

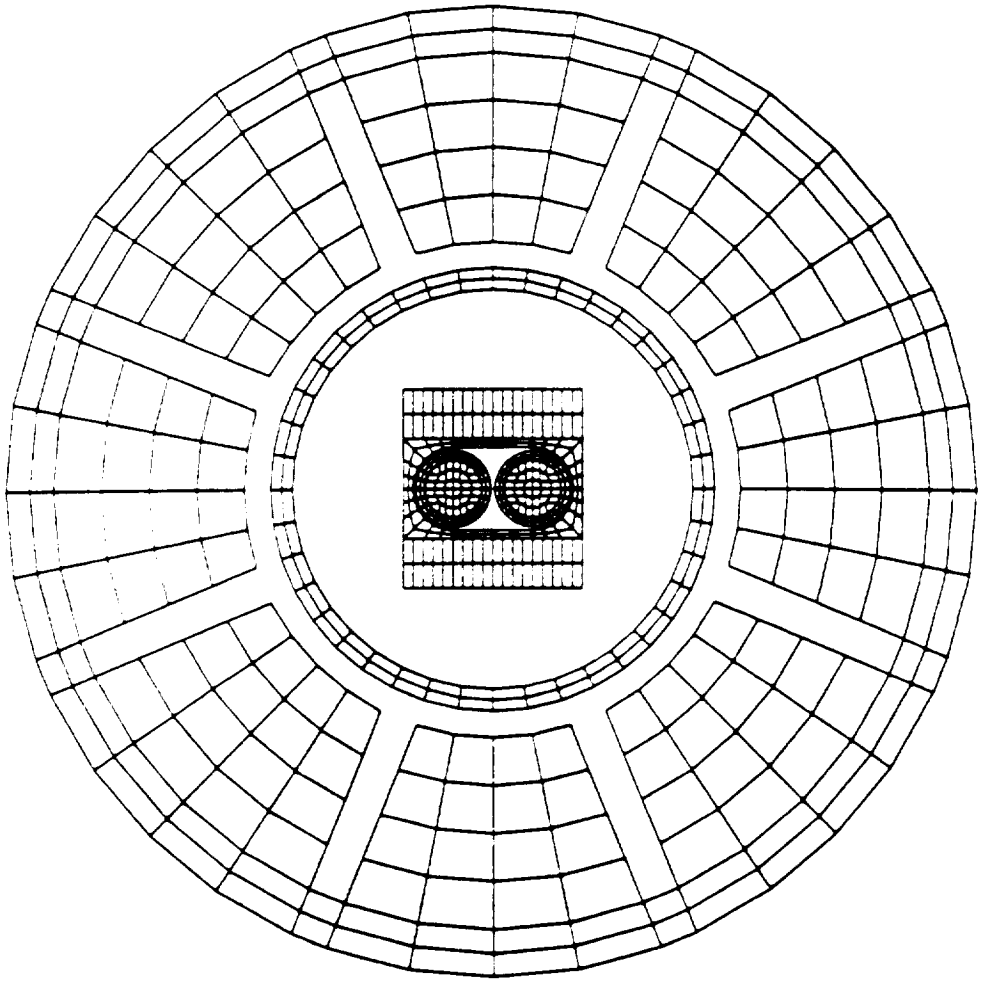

Figure 15. Initial GPHS Module Buffer Shield Geometry

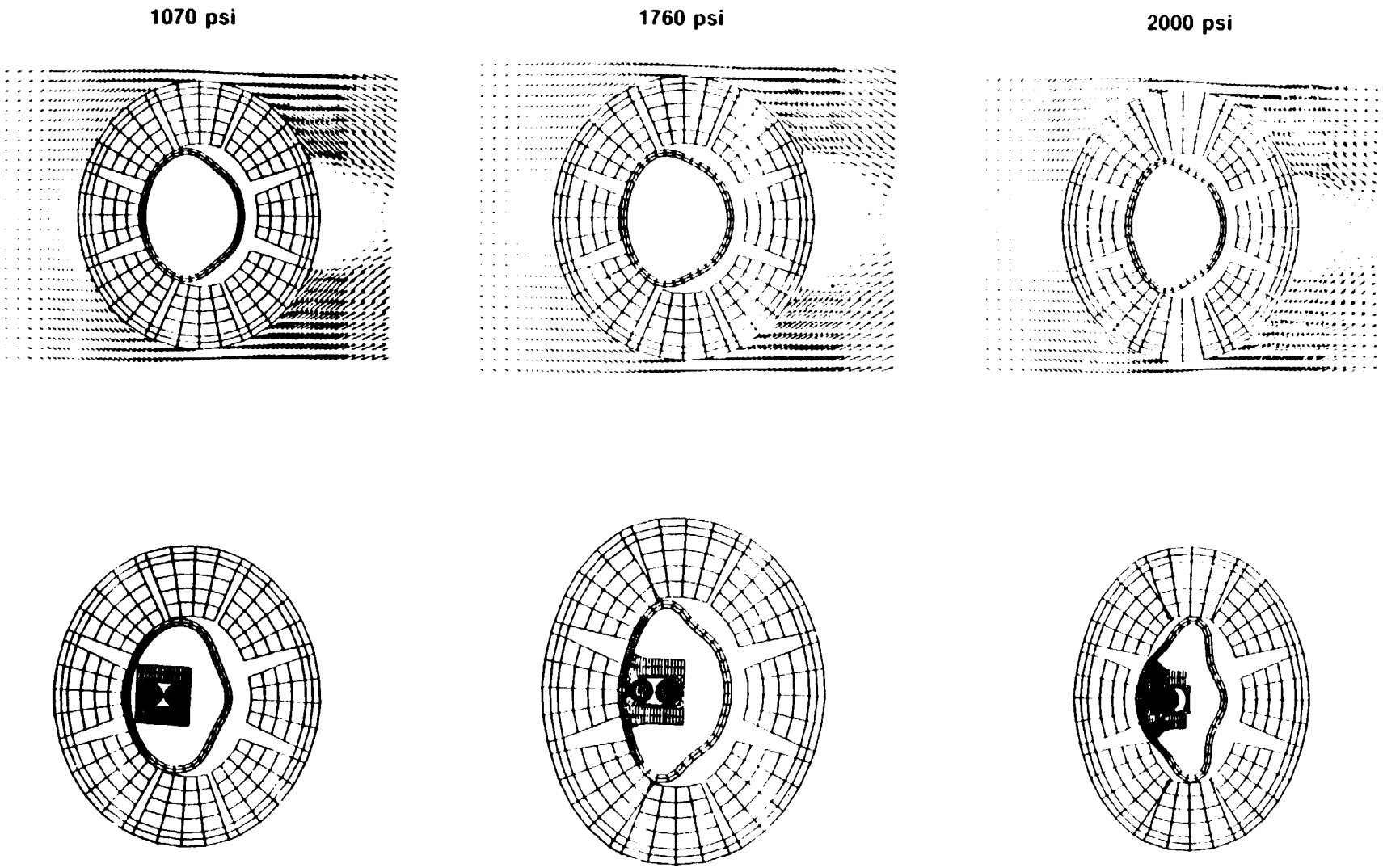

Figure 16. Buffer Shield Exposed to 1070 psi, 1760 psi and 2000 psi

where Ps is the density of the "matrix" material and ρ is the overall material density. The two values of α used were 7.869 for a honeycomb density of 22 lbs/ft^3 and 17.31 for a honeycomb density of 10 lbs/ft^3.

A quadratic form of the compaction curve is assumed for the honeycomb material.

$$g = 1 + [\alpha_0 - 1] \cdot \left[\frac{P_c - P}{P_c - P_e}\right]^2 \tag{6}$$

where: α_0 is the initial value of α and

g is the Herrmann quadratic [9].

The pressure at the elastic limit is Pe = 344 bars and the compaction pressure is P_c = 482 bars. Compaction begins when the pressure in the material P = Pe and ends when $P \geq P_c$.

Figure 17 depicts the GPHS module surrounded by its housing and a honeycomb shield. Figure 18 shows the honeycomb shield (density 22 lbs/ft^3) and its contents being exposed to loadings of 495 psi and 2000 psi. The shield would maintain its integrity at 495 psi but would definitely fail at 2000 psi. Figure 19 depicts a comparative response of the GPHS module for a honeycomb density of 10 lbs/ft^3 and 22 lbs/ft^3. The stiffer honeycomb offers better protection to the housing but causes a somewhat higher distortion of the iridium.

Figure 20 is a measure of the percentage ellipticity of the shields as a function of time for the two types of shields. The lower density shield has a slightly higher ellipticity than that of the higher density honeycomb.

Further calculations to illustrate the efficacy of the shield against fragments were made. A 0.5 inch thick steel fragment of an SRB was allowed to impact the shield and housing at 100 m/s. Additionally the fragment was allowed to impact the bare housing at the same velocity. The results are shown in Figures 21 and 22. Examination of these figures indicates the shield does mitigate the insult suffered by the housing due to fragment impact.

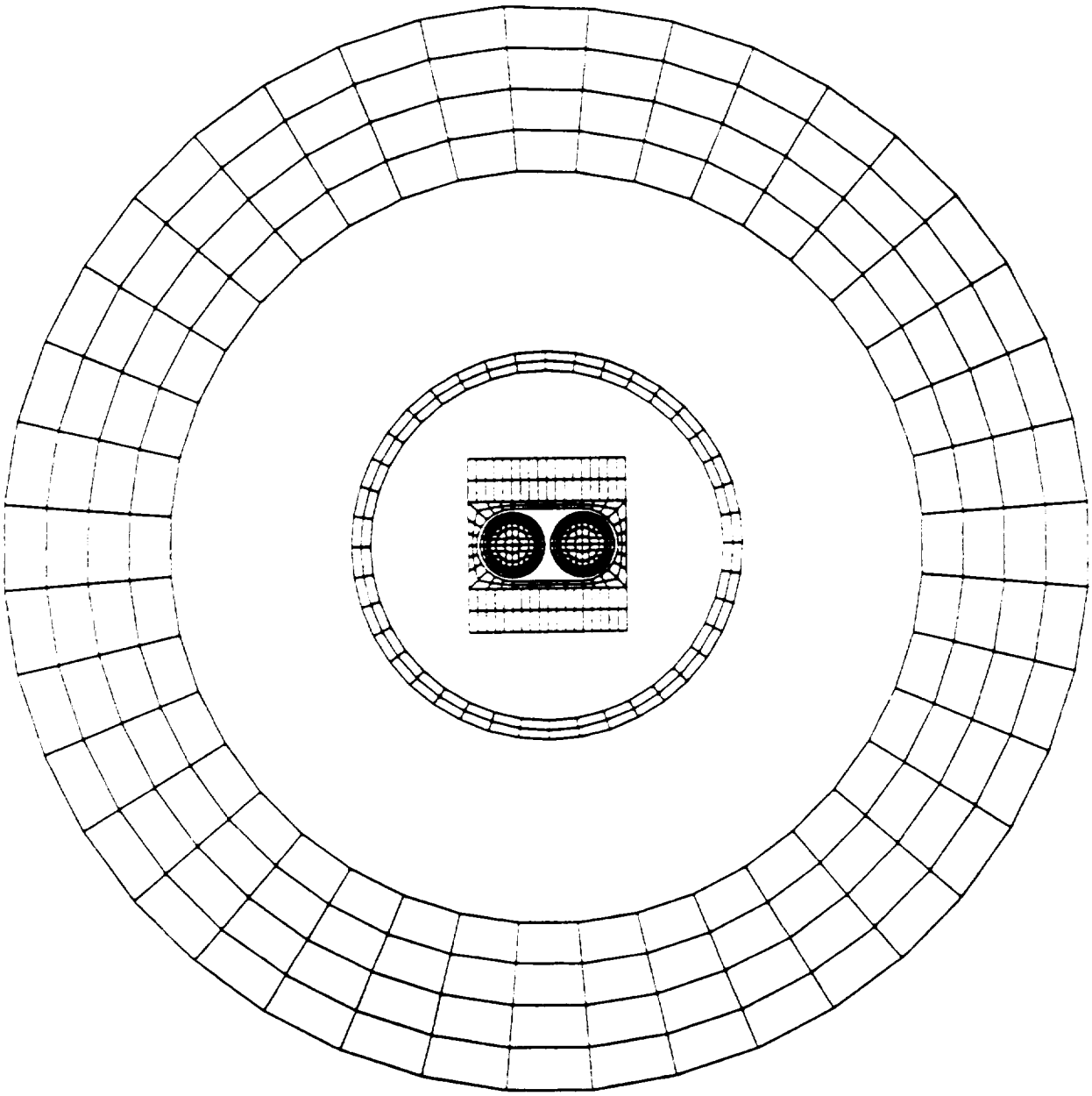

Figure 17. Initial GPHS Module Honeycomb Shield Geometry

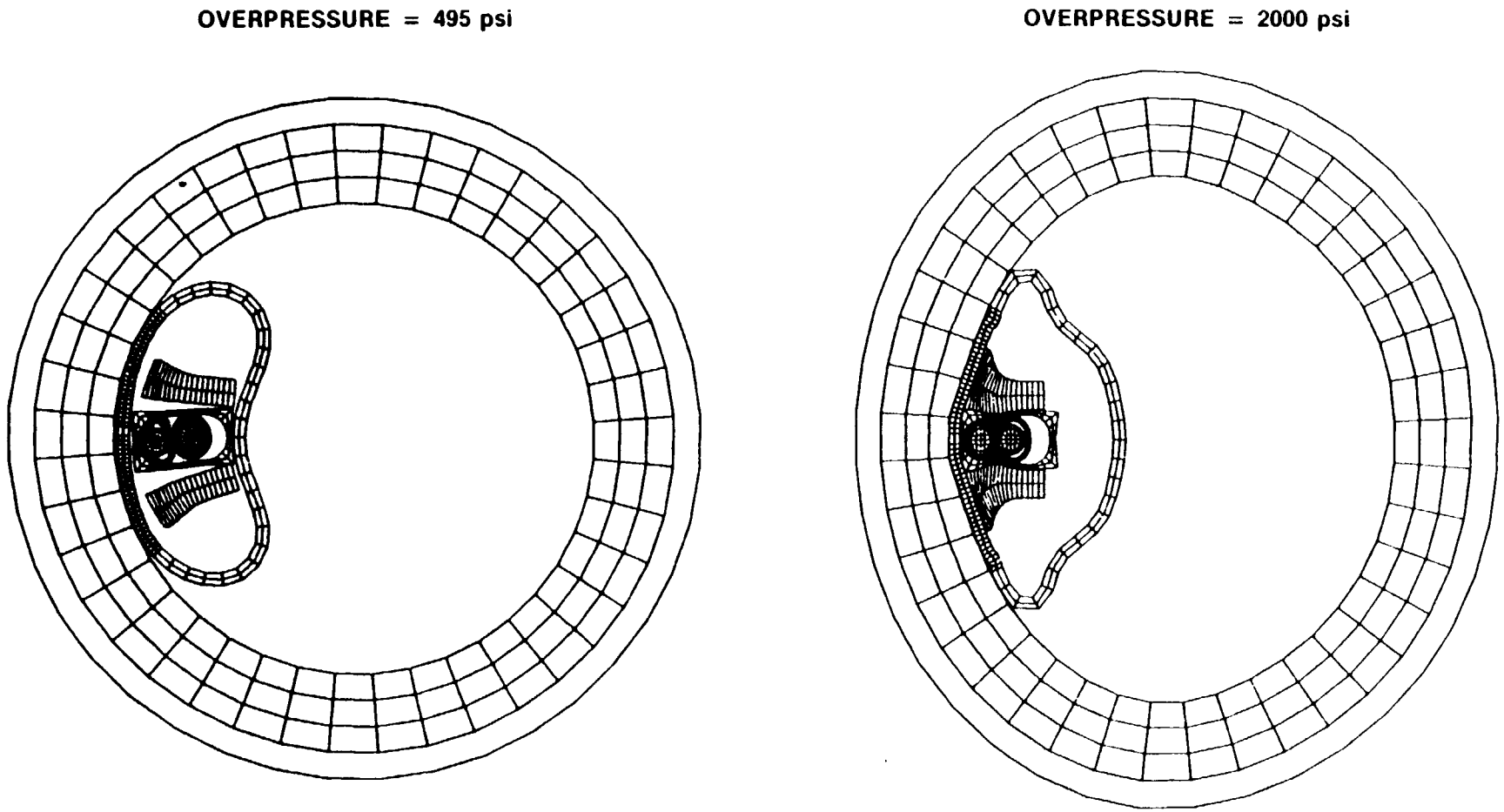

Figure 18. Comparison of Response of GPHS and Shield to Overpressures of 495 psi and 2000 psi

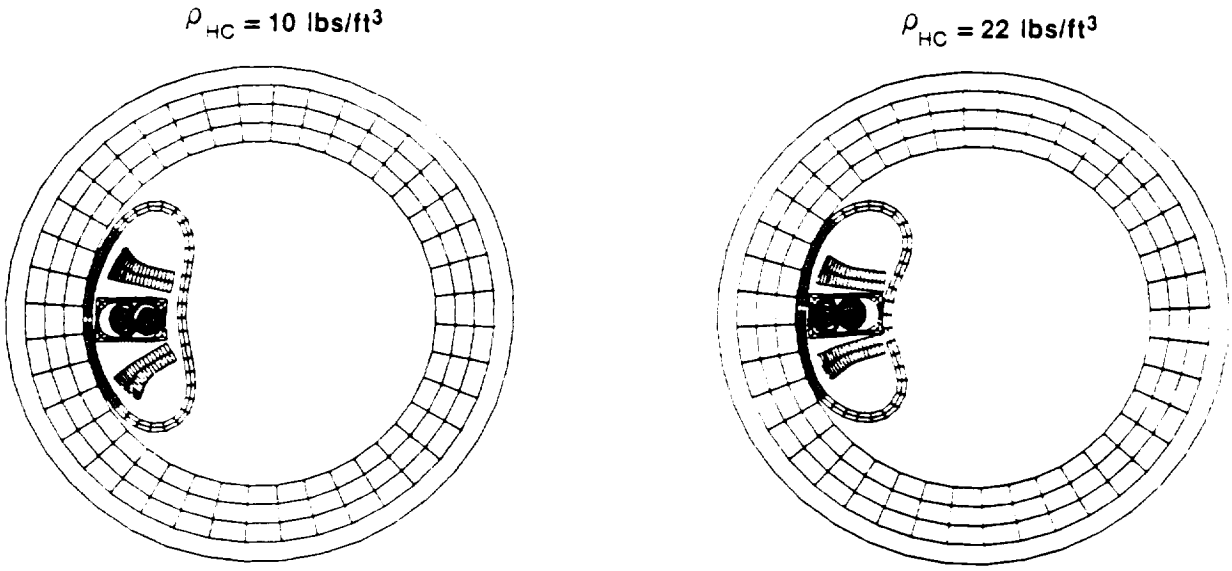

Figure 19. Comparison of Response for the Two Shields Proposed by JPL

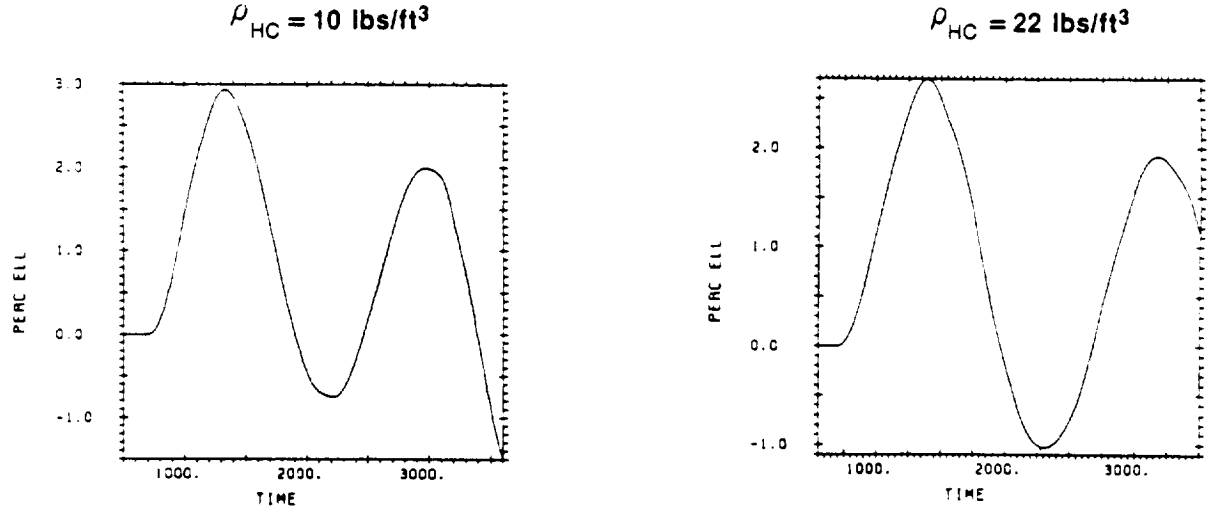

Figure 20. Comparison of Ellipticities

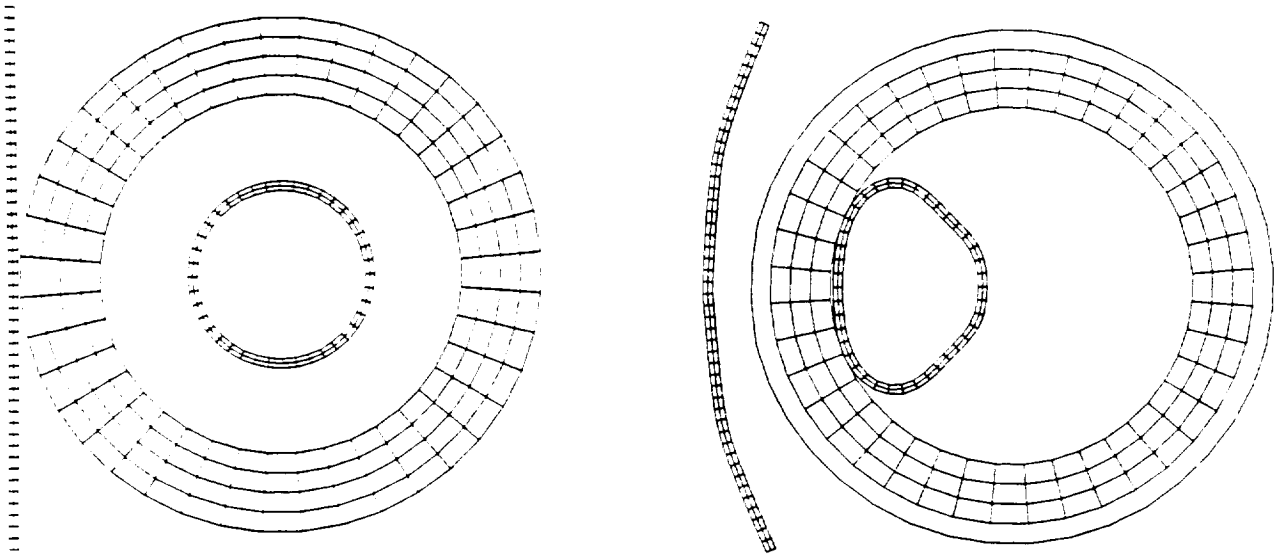

Figure 21. SRB Impacts Shield at 100 m/s

Figure 22. SRB Impacts GPHS at 100 m/s

Strong evidence was developed that the GPHS aeroshell would be damaged by impact between the various shield housing aeroshell interfaces. This implied that even at low overpressures, the shield would become the primary re-entry protection. This is, of course, unacceptable.

IV. STS 51L EXTERNAL TANK BREAKUP

The study described in this section includes the details of the calculations performed to predict the expansion of the cryogens stored in the 51L external tank (ET), subsequent to the ET failure.

These calculations were based on the following abort scenario:

1) Burn thru of the right SRB rear strut allowed the SRB to rotate about the forward attachment point.

2) This rotation torqued the cross beam and LOX tank causing the lower LOX tank dome weld to unzip.

3) The LOX tank minus its aft dome was driven forward by expanding oxygen and was broken up by aerodynamic forces.

4) LOX continued to move along the flight trajectory at Mach 2 in an expanding cone which continued to flow over the LH_2 tank for 56 msec until LH_2 tank break-up.

5) The LH_2 tank which had been leaking from an ~8 inch diameter burn-thru near the aft dome failed due to the application of unsustainable aerodynamic forces.

6) Late time (>200 msec) LH_2 release was essentially symmetrical about the flight vector. LH_2 expansion was initially assumed to be due to its stored internal energy.

7) The cloud resulting from this scenario was smaller in diameter than was recorded photographically.

8) Burning of hydrogen in low density air probably accounted for the greater than predicted cloud diameter.

The above scenario is consistent with the physical evidence obtained from:

1) Examination of the wreckage
   a) Bend direction of crossbeam
   b) Condition of aft LOX tank dome
   c) Impact marks of orbiter and right SRB on ET
2) Accelerometer in the orbiter
3) Ullage pressure measurements

There is no physical evidence that the LH_2 tank aft dome failed prior to the general break-up of the LH_2 tank. It should be noted that LH_2 will liquefy oxygen from air when released in the quantities and at the pressure that existed at MET 73 seconds. Any massive leakage which occurred prior to LOX tank failure would have evidenced itself as a white plume of liquefied oxygen droplets. No such plume was observed in any of the 51L photographs.

A. Assumptions

The calculations were performed to determine the magnitude of the cloud which would result solely from the isentropic expansion of the cryogens stored in the 51L external tank (ET). The analysis was done in three phases. The first phase entailed the calculation of the flight flow field which existed prior to the release of the cryogens. The pressure and density of the air at 50 thousand feet was employed to compute the flow field using the Eulerian processor in the continuum mechanics PISCES code. The ET was modelled as a rigid body accelerating at 2 g with a mass of 606,740 kg and moving at a velocity of 1803 ft/sec. The bow shock wave thus created was fully developed prior to cryogen release. The field developed around the ET is shown in Figure 23.

In the second phase, the wall of the liquid oxygen tank was modelled with a shell processor in the PISCES code and a two phase equation of state was developed for the liquid oxygen in the following manner.

The section of isentrope between boiling liquid at 1 atm and frozen O_2 is fitted with a quadratic [10]:

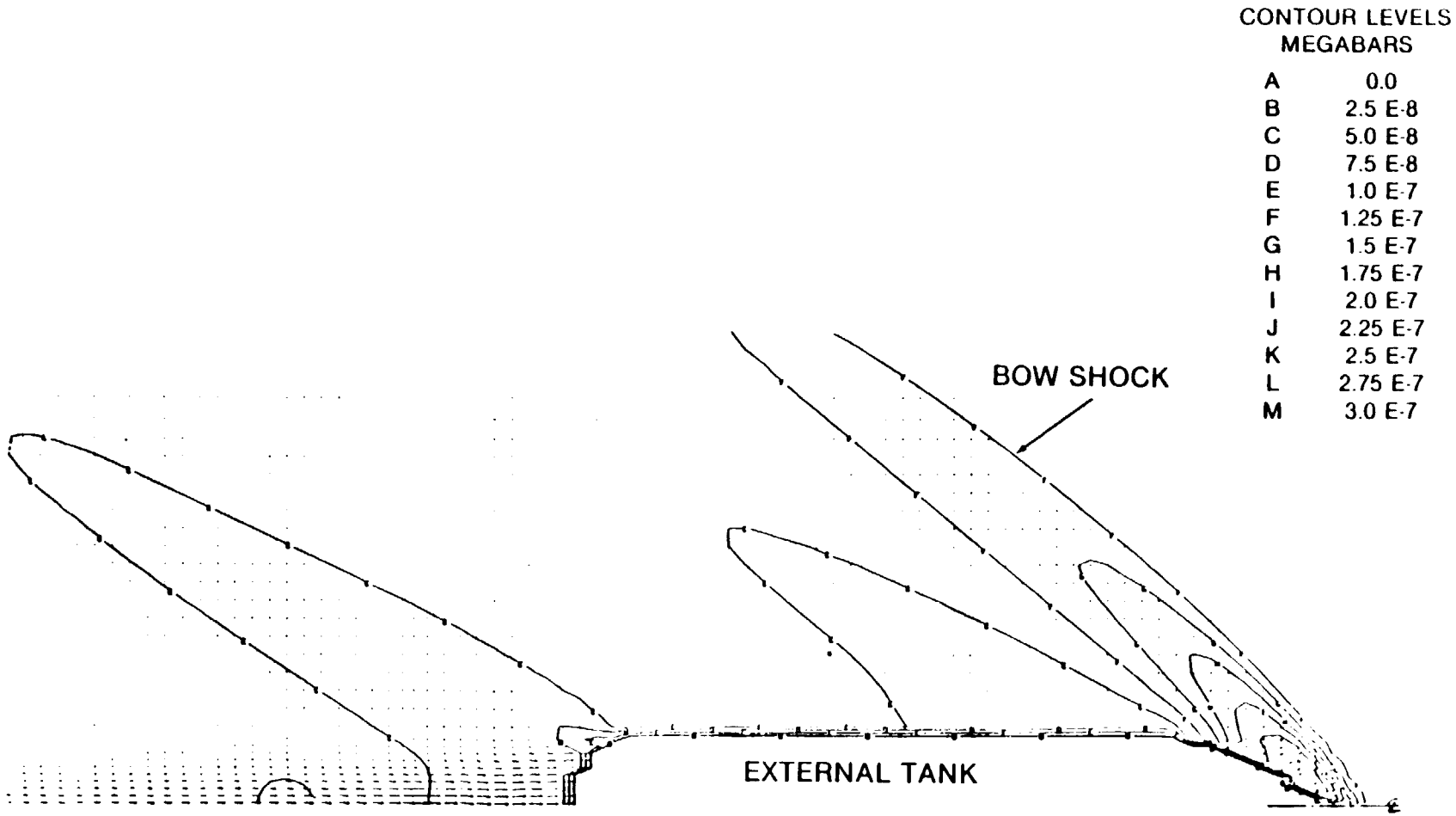

Figure 23. Flow Field Around External Tank Just Prior to LOX Tank Failure

$$P = A\,[lnV]^2 + B\,[lnV] + C \tag{7}$$

where:

A = -0.06062029

B = -0.07863105

C = 0.003791101

V = specific volume = $(1/\rho)$

The vapor solid region is fitted within an ideal gas isentrope

$$P = P_f\,(V_f/V)^{1.4} \tag{8}$$

where: P_f = freezing pressure = .00151 E6 dyne/cm^2

V_f = specific volume at freezing = 16840.0 cm^3/gm

The shell processor coupled the LOX tank to the atmospheric air at 50,000 feet on the outside and to the expanding oxygen on the inside. Both the air and the oxygen are modelled using the Eulerian processor embedded in the code.

Figure 24 shows the relative position of the LOX and LH_2 just prior to LH_2 tank failure and depicts the liquid oxygen moving over the liquid hydrogen tank just prior to its failure.

Figure 25 shows the initial surge of LH_2 to form what has been called the "explosion doughnut." This figure shows that it is not necessary to have an explosion to create an expanding material interface having the dimensions and velocity observed in the photographic records of the 51L event.

In the third phase of the event, the liquid hydrogen was modelled using a two phase equation of state developed by Lehto [10]. This "primary" expansion isentrope is shown in Figure 26 and is easily constructed from the saturation conditions [11, 12]; the section of isentrope between boiling liquid at 1 atm and frozen hydrogen is fit with a quadratic.

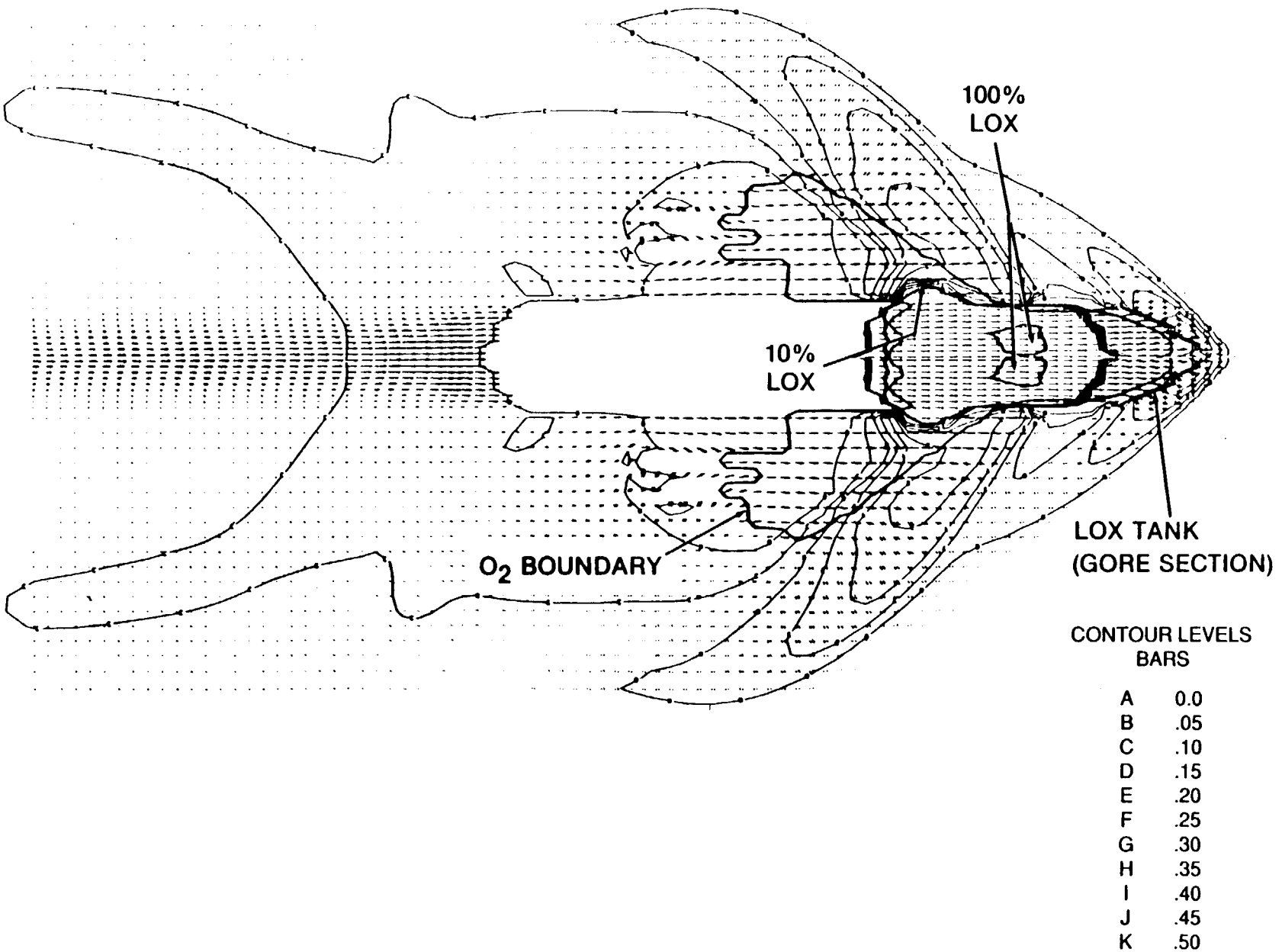

Figure 24. Material Location 56 mSEC After LOX Tank Failure

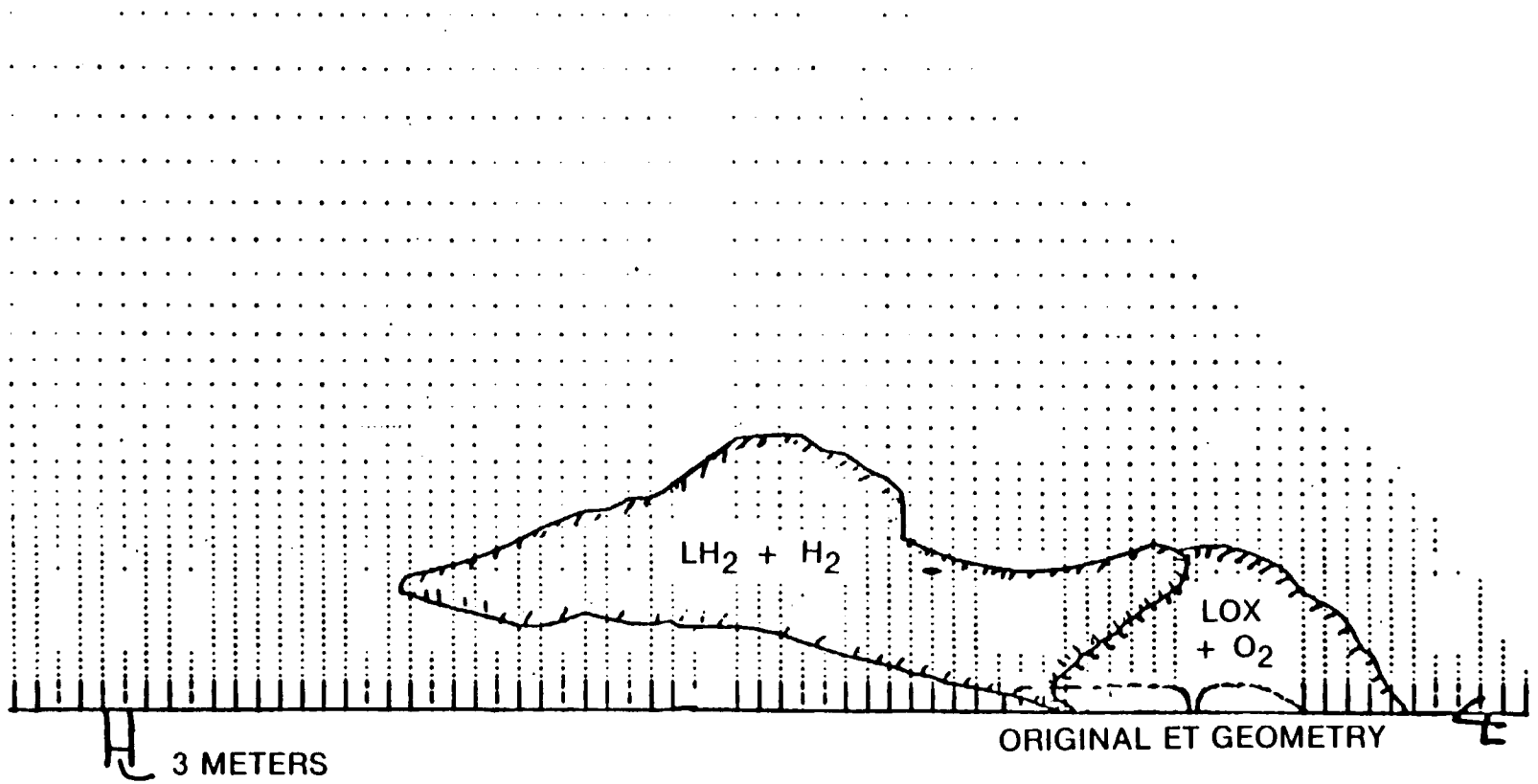

Figure 25. Cryogen Contact Surfaces 400 mSEC After LOX Tank Failure

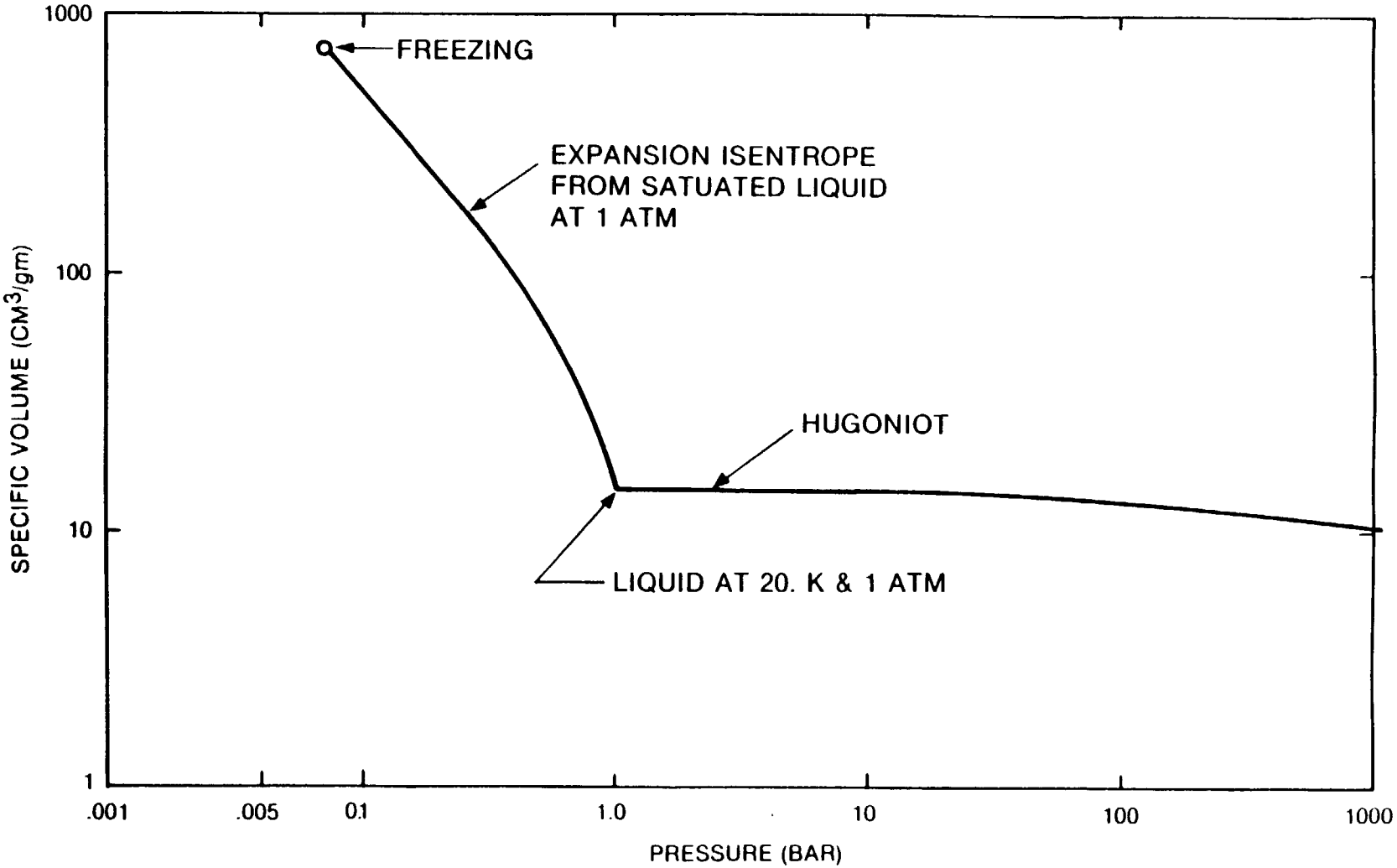

Figure 26. Expansion Isentrope for Liquid H_2

$$\ln P = A (\ln V)^2 + B (\ln V) + C, \quad (9)$$

where:

$A = -9.345068E\text{-}2$

$B = 0.20633173$

$C = 0.11216199$

V = specific volume (cm^3/g) = $1/d$

In the vapor-solid region, a simple ideal-gas isentrope is used:

$$P = P_f (V_f/V)^{1.4} \quad (10)$$

P_f = freezing pressure = 0.072E6 dyne/cm^2 (.072 bars)

V_f = specific volume at freezing = 760 cm^3/g.

The equation of state assumes liquid-gas equilibrium at an initial ullage pressure of 34 psia. Subsequent isentropic expansion of hydrogen, including the work done in accelerating the liquid in the two-phase mixture was modelled.

Cloud expansion is well under way 440 msec after LH_2 tank failure. The so called "explosion doughnut" is already clearly defined as shown in Figure 25. A rough scale drawing of the original ET dimensions is included in the figure for reference. The continuing bow shock and flow field development around the expanding cryogen is shown in Figure 27, 440 msec after LH2 tank failure.

Similar plots of material location and flow field development 712 msec after LH_2 tank failure are presented in Figures 28 and 29. Figure 30 shows a comparison between the predicted cryogen cloud development and the optical data reduction performed by RDA [1]. Good agreement between predicted cloud size and cloud growth rate is obtained during most of the observation period. Late time under-prediction of the cloud diameter is probably due to the omission of heat input from the environment to the expanding cryogen and to H_2 deflagration. No attempt was made to model heat input from H_2 deflagration, LH_2-LOX-AIR mixing, or the SRB exhaust plume. Inclusion of these phenomena would have increased the predicted values for late time cloud diameter.

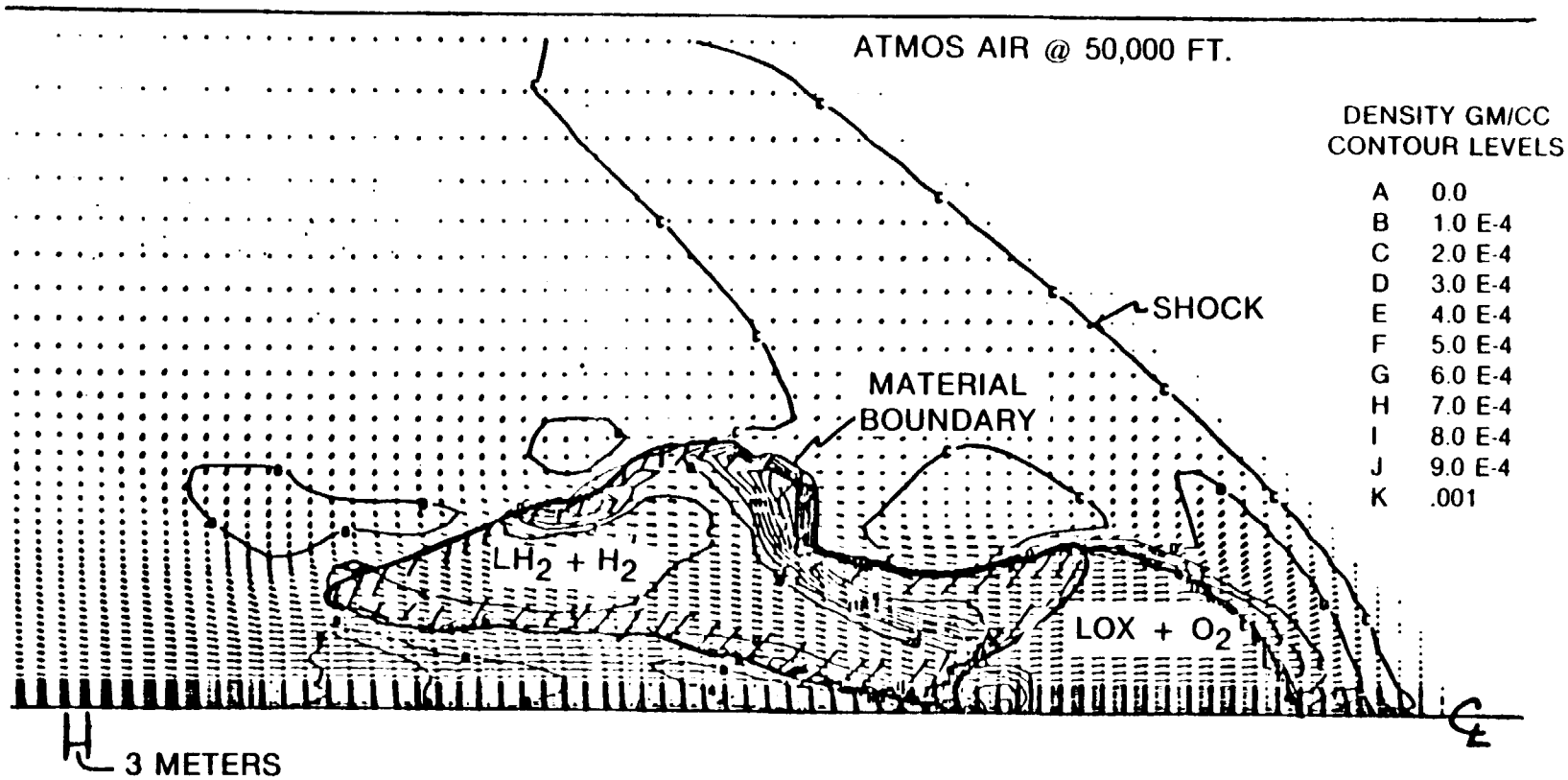

Figure 27. Flow Field Around Expanding Cryogens 400 mSEC After LOX Tank Failure

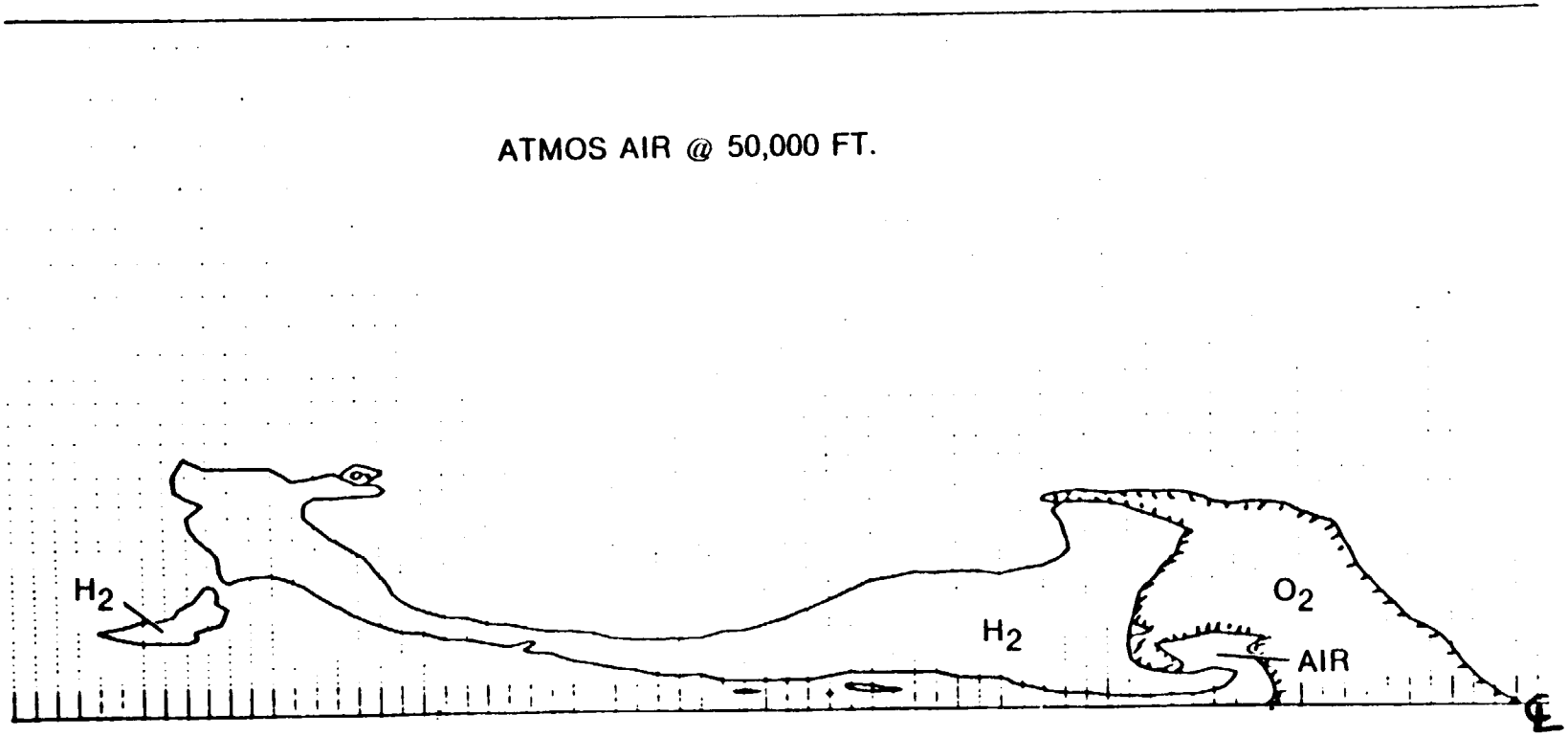

Figure 28. Cryogen Contact Surfaces 712 mSEC After LOX Tank Failure

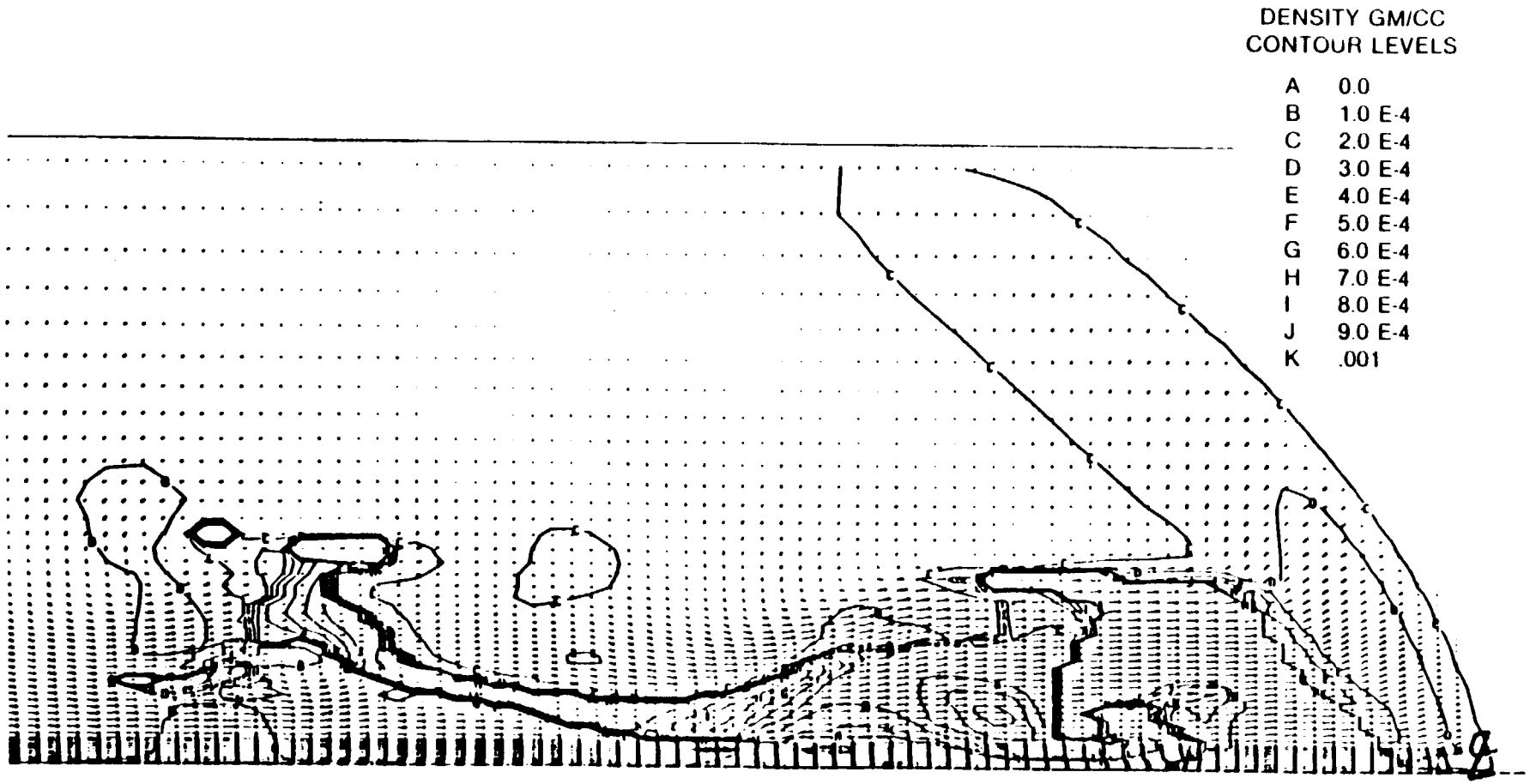

Figure 29. Flow Field Around Expanding Cryogens 712 mSEC After LOX Tank Failure

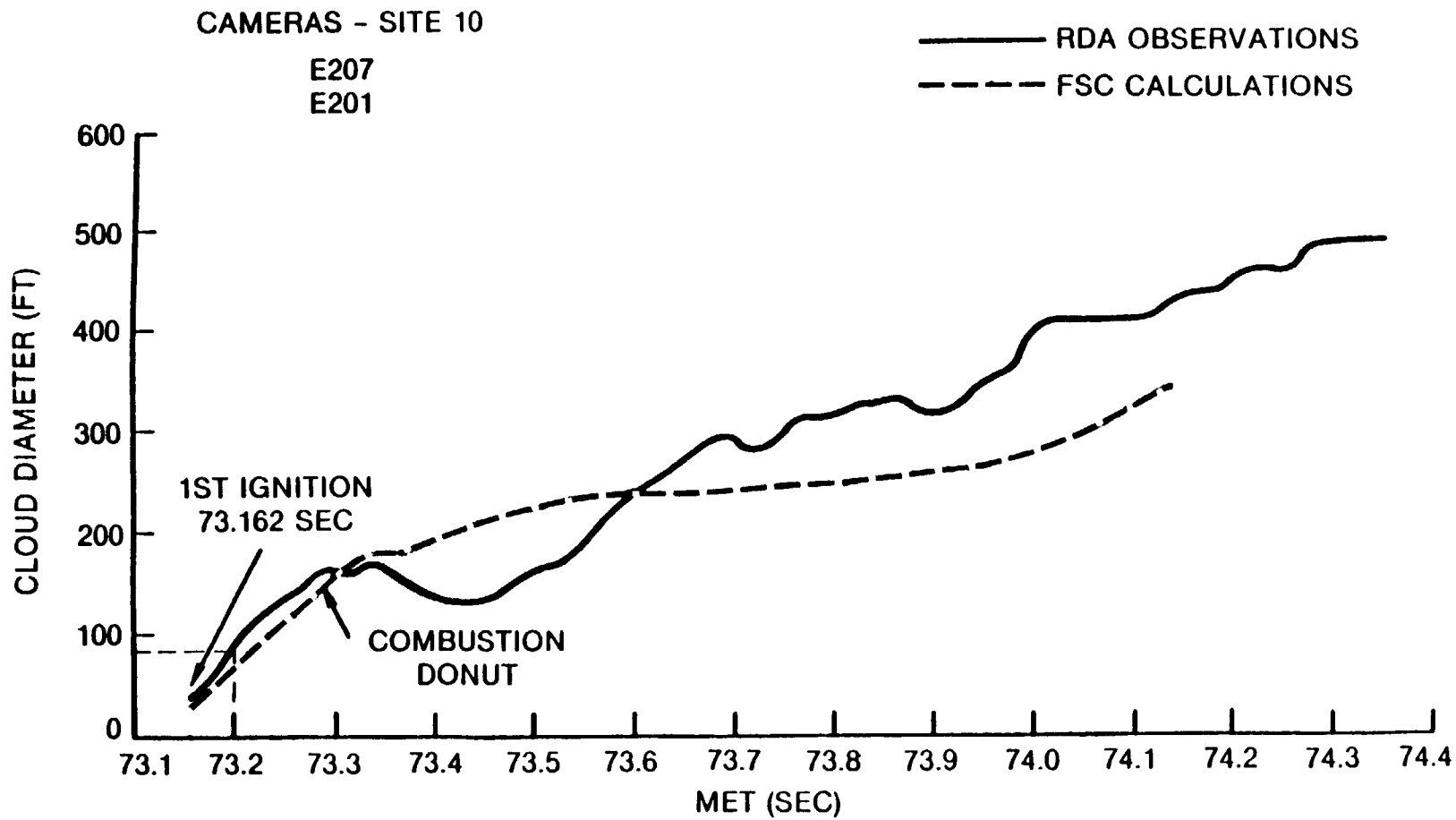

Figure 30. Cryogen Contact Surface Growth

V. ET SPILL CALCULATIONS

The study described in this section details the calculations performed by FSC personnel to simulate the impact of the STS external tank with the ground at a velocity of 100 ft/sec.

A two phase equation of state was developed for the liquid hydrogen at low temperatures. The model has a two phase saturation curve for para hydrogen since at low temperatures the composition is 99.8 percent para. Saturation data for hydrogen are given graphically [13] and a digitized representation of these data was developed for the two phases. Beneath the saturation curve, an iterative scheme is used to find the pressures. The iterative parameter is the vapor fraction, and the iteration adjusts the vapor fraction until an energy balance is achieved. At energies above the saturation curve, for a given density, a Mie Gruneisen extrapolation is used to estimate the pressure, using tabulated values of the Gruneisen parameter.

The material model is based upon the shock Hugoniot data for compression (relative to conditions at 1 atmospheric pressure and 20 K) and thermodynamic tabulations for expansion. Shock Hugoniotal data for liquid hydrogen are given in Marsh [14] for pressures up to 65 kbar and extended by Nellis et. al. [15] to 100 kbar. The initial conditions are:

ρ_0 = density = 0.072 g/cm^3
P_0 = pressure = 1 atmosphere
T_0 = temperature = 20 K
c_0 = sound speed - 1089 m/s

The lowest experimental pressure is about 20 kbar. In order to have a representation of the pressure range down to 1 atmosphere, a fit to the data was developed using the Murnaghan shock Hugoniot:

$$P = A\left[\left[\frac{\rho}{\rho_0}\right]^{\gamma} - 1\right] \tag{11}$$

where: $A = \frac{\rho_0 c_0^2}{\gamma}$

and: $k = 5.9$ (12)

A Gruneisen coefficient of 2.3 [12] was used to extend the equation of state to states which are off the Hugoniot.

An equation of state developed by Lehto [10] and described in the previous chapter was used for the LOX.

All the calculations were done in axial symmetry with the cryogens being modelled using the Euler processor in the PISCES code. The cryogens were assumed to have an initial velocity of 100 feet per second. All Euler cells are assumed to be adiabatic; i.e., there is no heat transfer between two components within a cell and no heat transfer between cells. This formulation will under predict the effects of mixing at the cryogen interface.

The calculations were made for each of the following boundary conditions:

a) ET intact at impact - where the cryogens were not allowed to expand before impact and,

b) ET failed before impact - where the cryogens were allowed to expand during impact.

For each of the boundary conditions described above, the following scenarios were analyzed.

a) ET nose first impact wherein the LOX tank impacted first followed by the LH_2 tank, and

b) ET aft first impact wherein the aft end of the LH_2 tank impacts first followed by the LOX tank.

Examination of the material presented in the Figures 31, 32 and 33 demonstrates that there will be a substantial expansion of the cryogens while falling to earth from even modest (gantry) heights. This expansion will tend to limit the density of the residual two phase cryogen which is available to accumulate and mix on the ground surface.

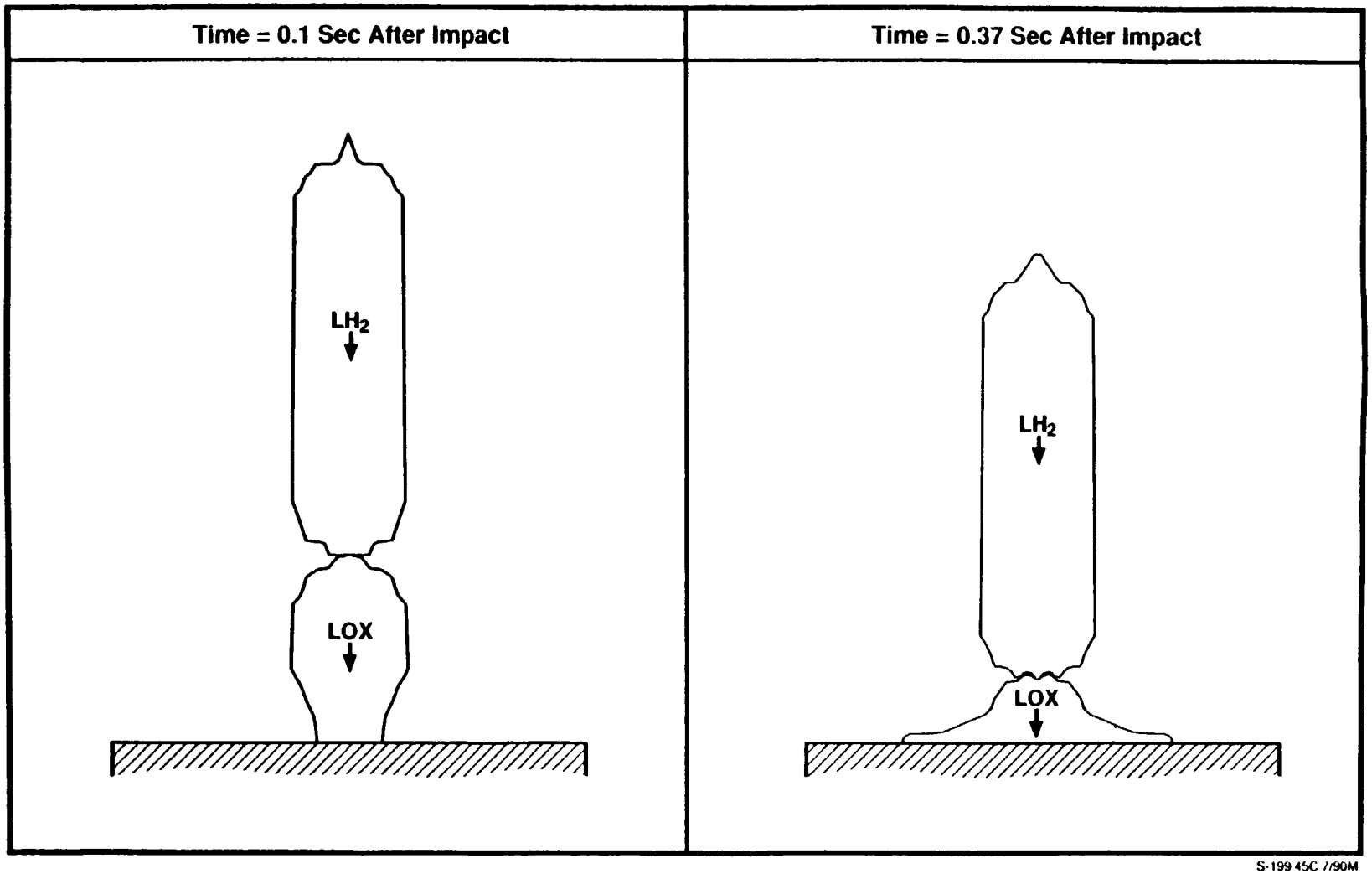

Figure 31. Profiles of Cryogens at 0.1 Sec and 0.37 Sec During Intact Impact of ET (Nose First)
ET Intact at Impact

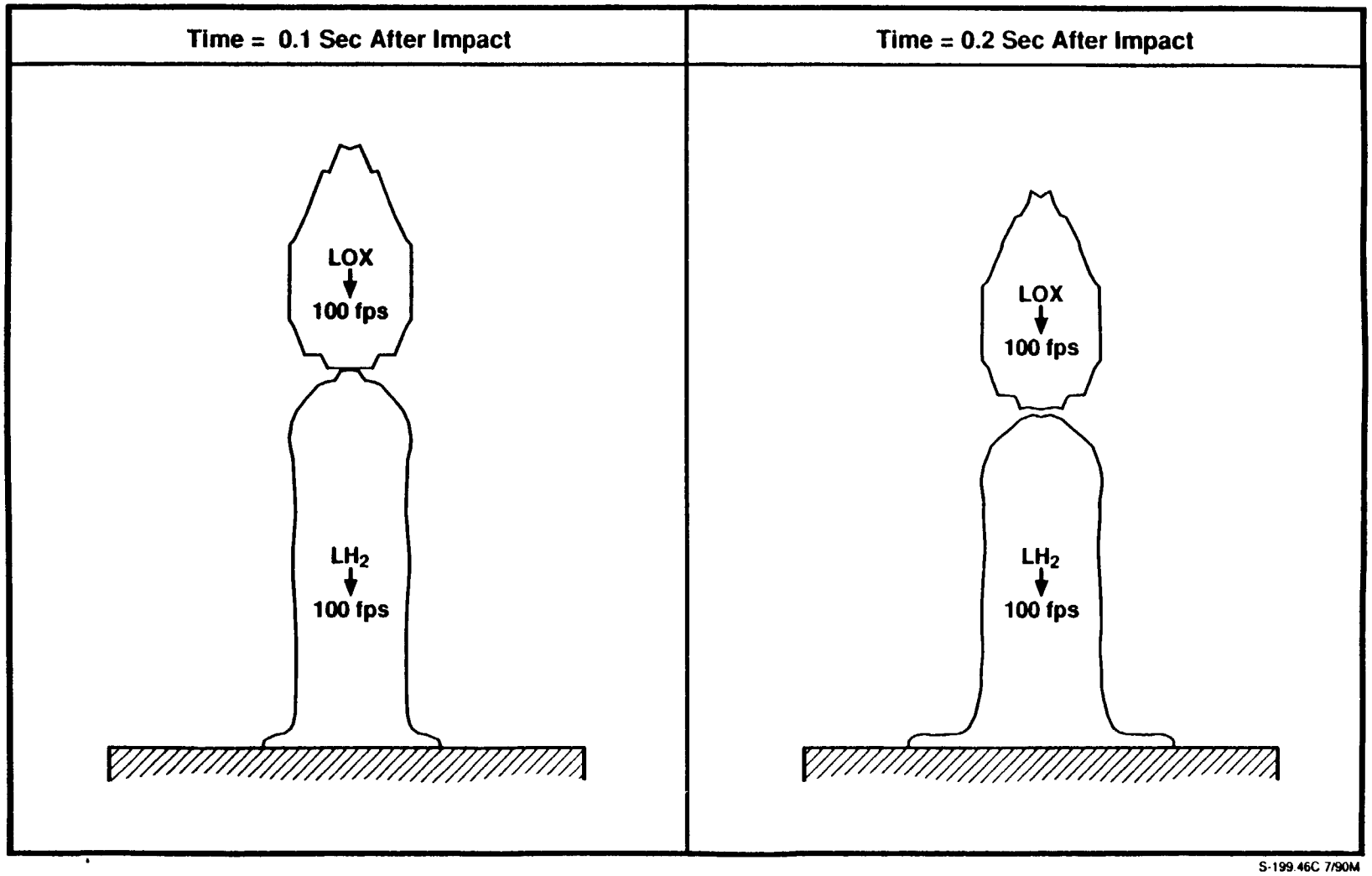

Figure 32. Profiles of Cryogens at 0.1 Sec and 0.2 Sec During Intact Impact of ET (Aft First)
ET Intact at Impact

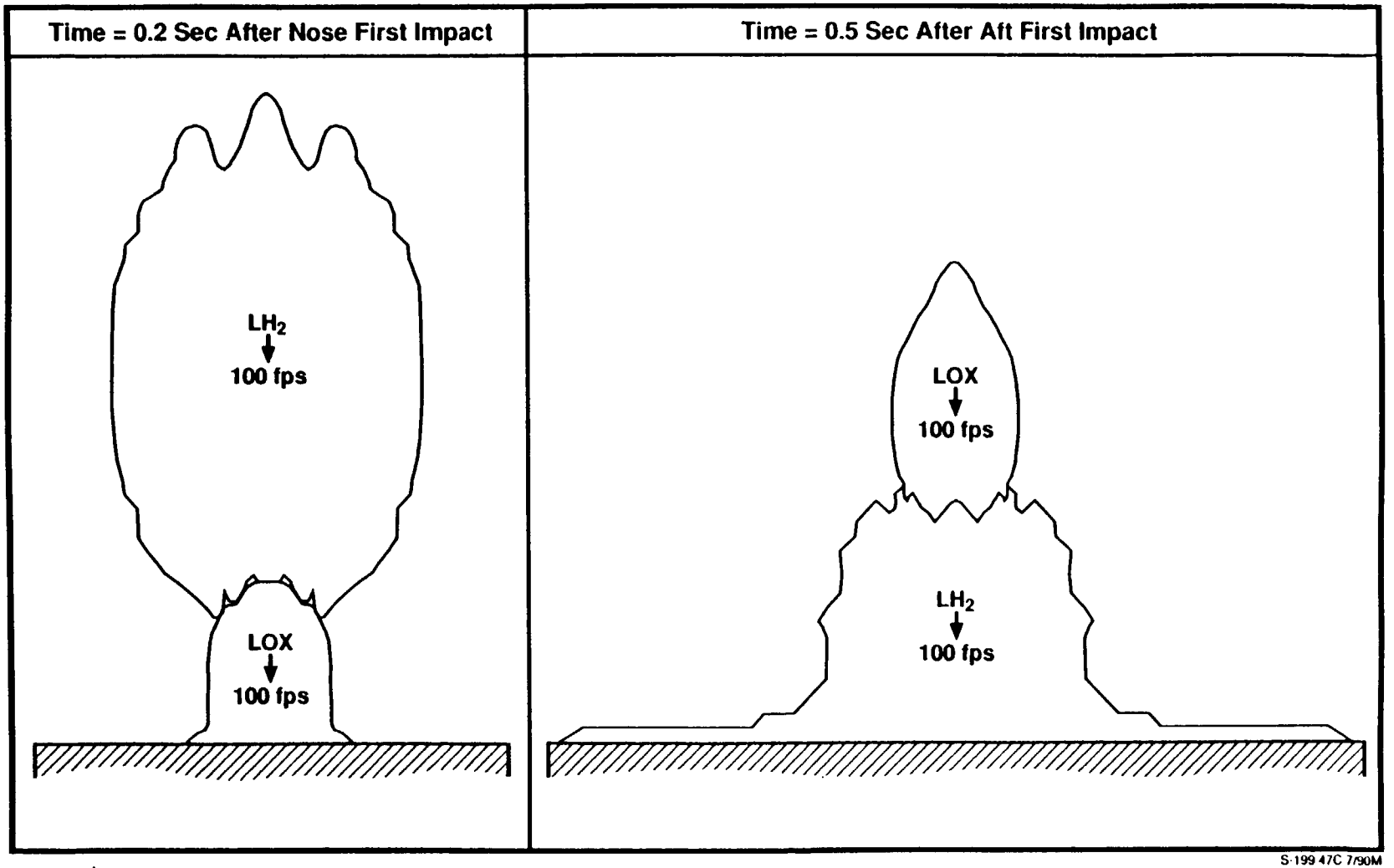

Figure 33. Comparisons of Expanding Cryogens During Nose First and Aft First Impact
ET Failed at Impact

VI. ORBITER RESPONSE TO SPILL BLAST

FSC personnel analyzed the response of the orbiter to a blast originating from a pool of LH_2 - LO^2 accumulated on the mobile launch platform. The Euler processor in the PISCES 2D ELK code was used to model a one foot deep pool of a mixture of liquid oxygen and liquid hydrogen in contact with the mobile launch platform. The mixture was assumed to detonate starting at the rigid surface. The analytical solution is well known [16] as the Taylor blast wave similarity solution. The program uses the equations described on the next page to initialize the zones in the pool to the appropriate values at the time that the detonation front reaches the pool/air interface.

The density of the mixture in the pool was assumed to be 0.0056 g/cm^3 with a specific internal energy of 1050 cals/g. The gas gamma of the reactants was assumed to be 1.3. The blast wave thus generated was moved through a distance of 10 meters by making use of a moving Euler grid capability available as a special user written subroutine in the code. Normally, Eulerian grids remain fixed in space. The dynamic rezoner capability allows the user to move or expand the Euler grid in order to track over a long distance, the development of the shock front created by an explosion.

The calculations involved a large number of restart runs with the shock front being carefully tracked within a moving Euler mesh. When the shock front was about 50 cm from the main engines, the detailed geometry, of the cargo bay doors and rigid body simulations of the space shuttle main engine and IUS were set up. The Euler grid was made stationery and the code coupled the gas in the Euler with the Lagrangian structures. Calculations were made for two different scenarios:

a) An axisymmetric bay model having its axis parallel to the flow field and,
b) A translational symmetry model having its axis normal to the flow field

The three space shuttle main engines (6950 lb each) were modelled as a wall using the 2D ELK rigid body processor. The total loaded weight of SRM-1 and SRM-2 in the IUS is 29596 lbs and the probe weighs 1324 lbs. These were modelled as rigid bodies having a combined

Equations for Detonation Wave

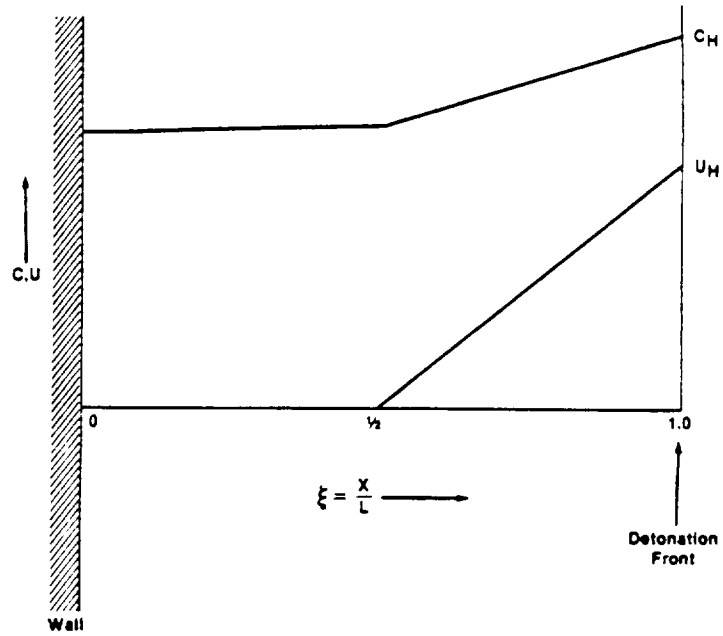

L = length of reactants consumed by detonation

ρ_o = initial density

e_o = chemical energy per unit mass

γ = effective gas gamma

$$D = \sqrt{2(\gamma^2 - 1)e_o} = \text{detonation speed}$$

$$u_H = \frac{D}{\gamma + 1} = \text{C - J velocity}$$

$$c_H = \gamma u_H = \text{C - J sound speed}$$

$$\xi = \frac{X}{L} = \text{dimensionless distance from wall}$$

$$u = \begin{bmatrix} \mu_H(2\xi - 1) & \text{if} \quad \frac{1}{2} \le \xi \le 1 \\ 0 & \text{if} \quad 0 \le \xi \le \frac{1}{2} \end{bmatrix}$$

$$c = \begin{bmatrix} \frac{c_H}{\gamma}((\gamma - 1)\xi + 1) & \text{if} \quad \frac{1}{2} \le \xi \le 1 \\ D/2 & \text{if} \quad 0 \le \xi \le 1 \end{bmatrix}$$

$$\rho = \rho_H\left(\frac{c}{c_H}\right)^{2/(\gamma-1)} \text{ where } \rho_H = \frac{\gamma + 1}{\gamma}\rho_0$$

weight of 30,920 lbs. The cargo bay doors were modelled using the shell processor embedded in the PISCES code.

The strain in the cargo bay doors due to interaction with the shock front was monitored. When the predicted strain exceeded the failure strain of aluminum, appropriate sections of the door were made transparent to the flow. Figure 34 depicts a typical result of the calculation in the axisymmetric model. The axis of the bay is parallel to the flow field which interacts first with the heavy engines (solid wall) before impacting the bay door.

Figures 35, 36 and 37 are results showing the pressure contours around the cargo bay and the resulting inward motion of the bay doors. The bay doors were calculated to move inwards at a velocity of 60 m/s. Figure 38 indicates the magnitude of the pressures extending along the length of the bay above and below the doors - a pressure of about 4 bars outside and 2 bars inside the bay.

Figure 39 depicts typical results of the calculations in the translational symmetry mode. In this case the axis of the bay is normal to the flow field which interacts directly with the cargo bay doors. This resulted in an implosion of the bay doors shown in Figure 40. They were calculated to be moving at a velocity of 100 m/s.

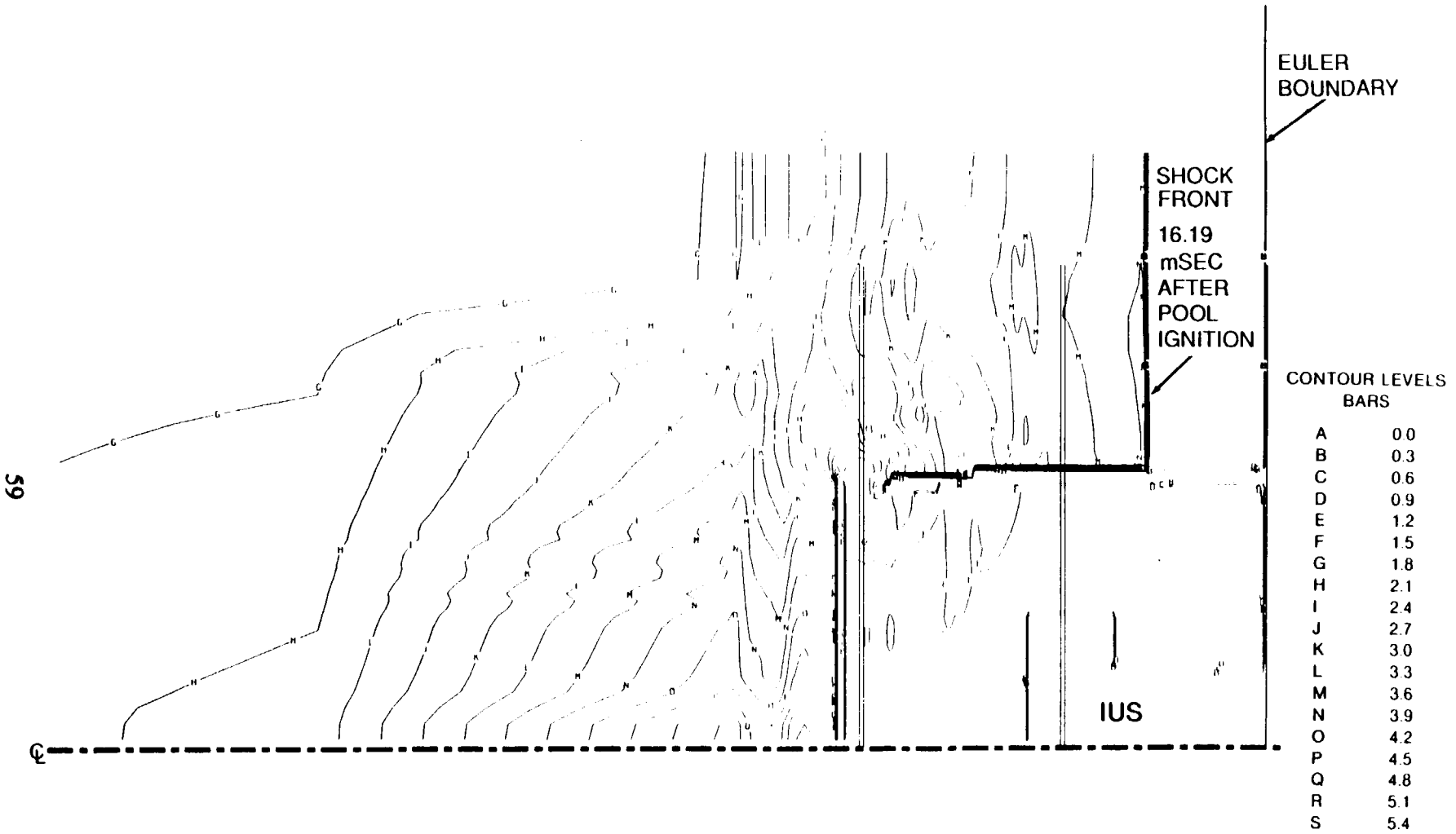

Figure 34. Pressure Extant Around SSME and Cargo Bay (Axis Parallel to Flow Field)

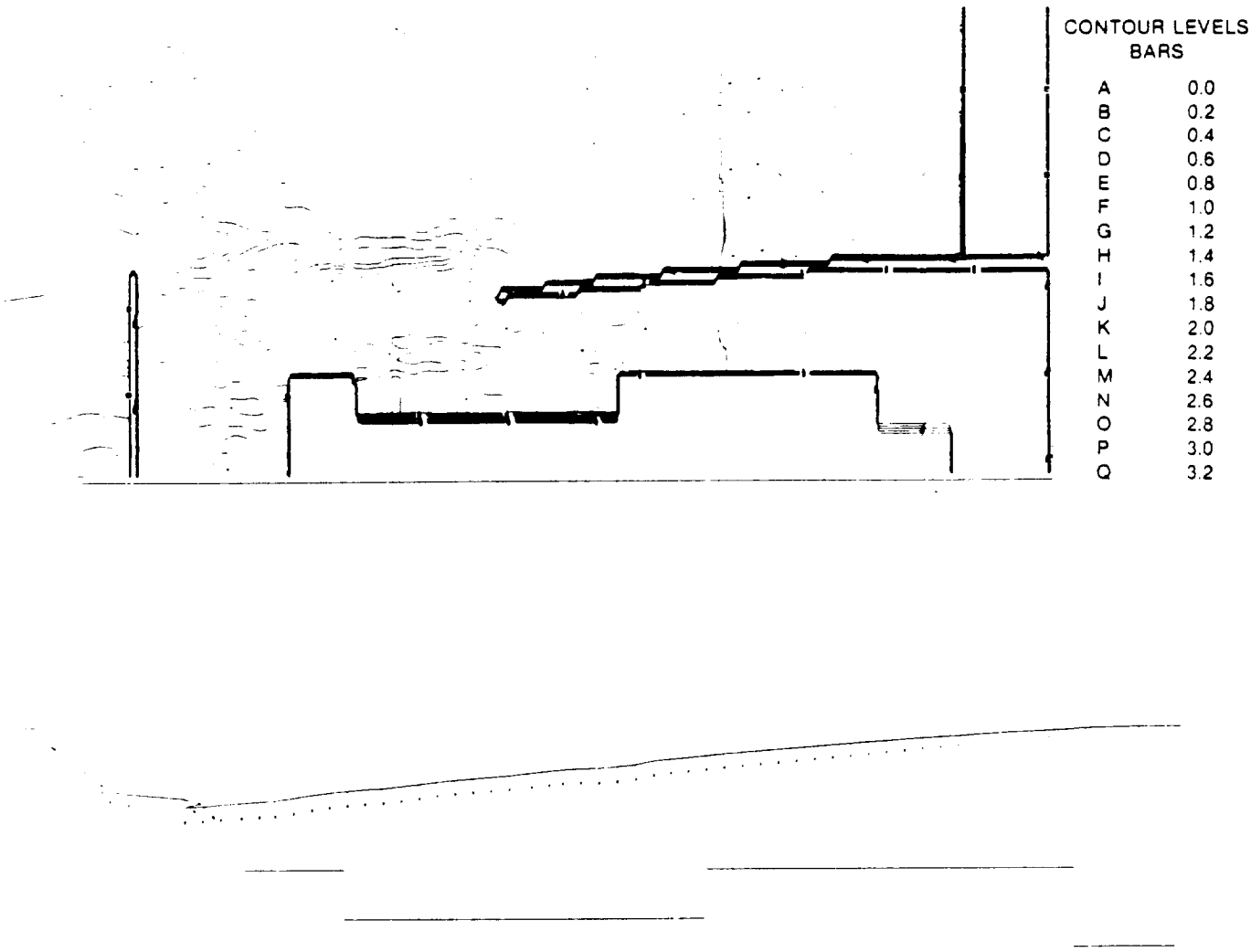

Figure 35. Pressure Contours and Velocity Vectors of Cargo Bay Door at 27.4 mSEC

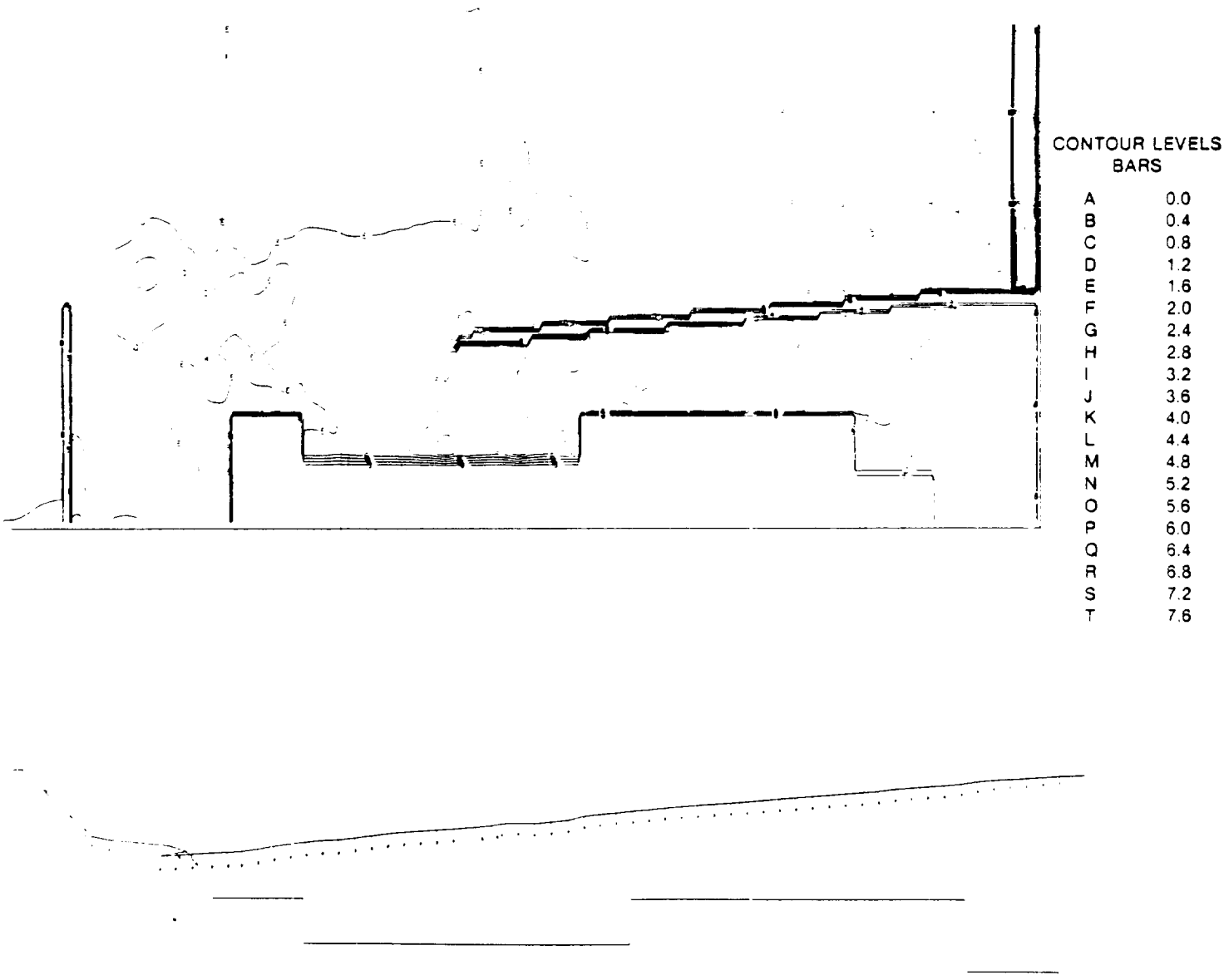

Figure 36. Pressure Contours and Velocity Vectors of Cargo Bay Doors at 30 mSEC

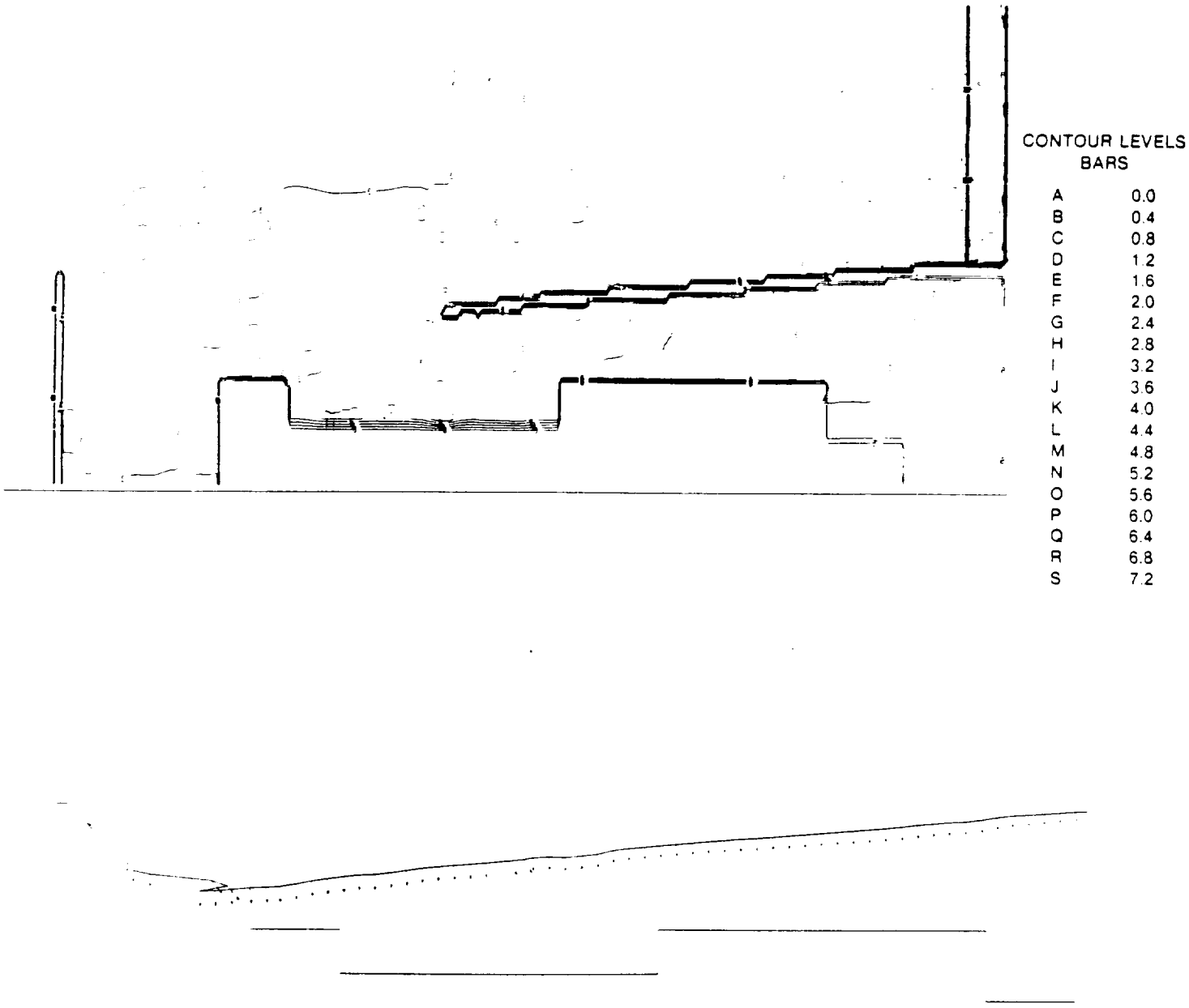

Figure 37. Pressure Contours and Velocity Vectors of Cargo Bay Doors at 30.5 mSEC

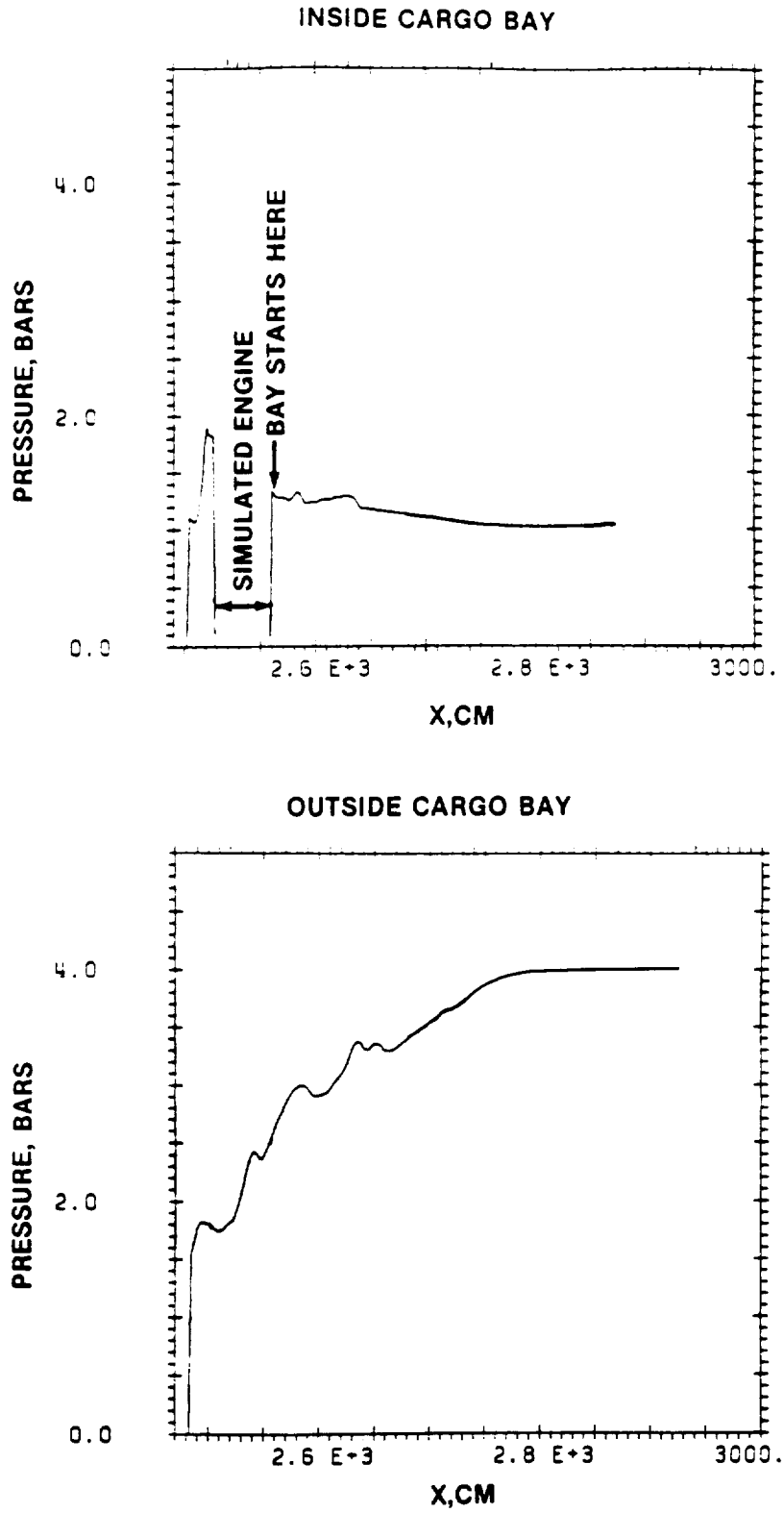

Figure 38. Pressure Extant Inside and Outside Cargo Bay

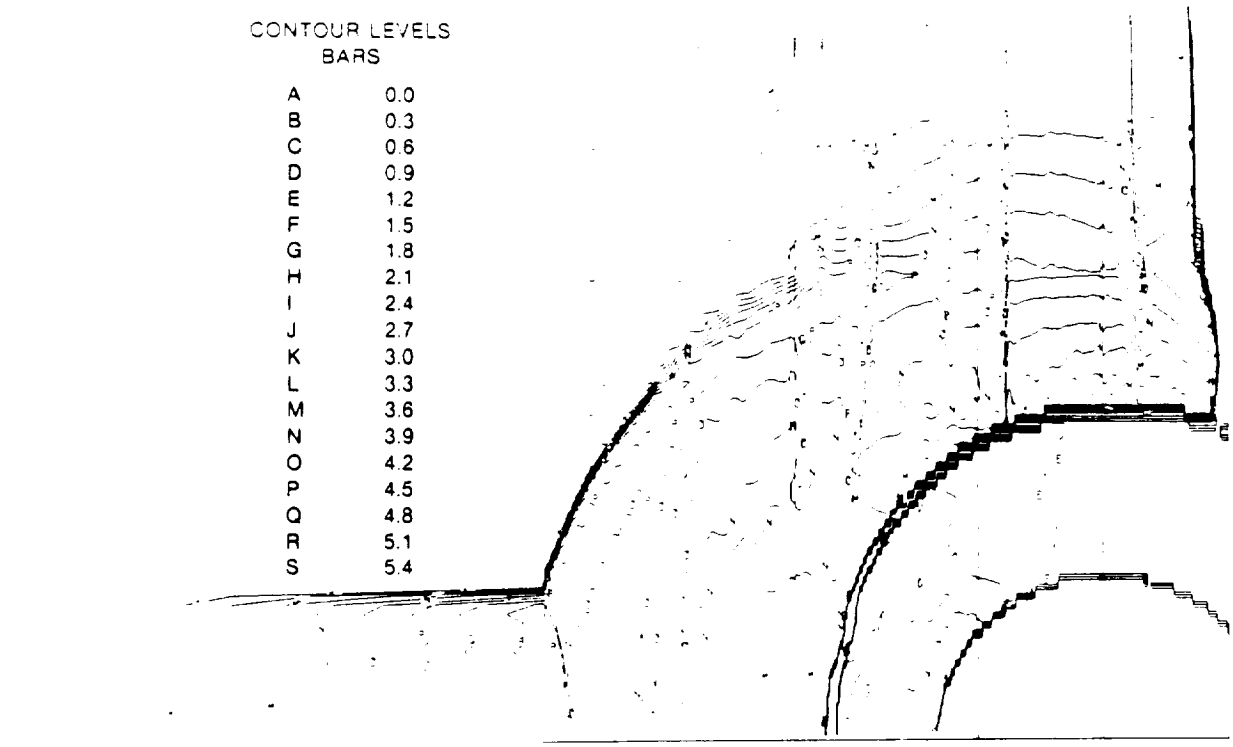

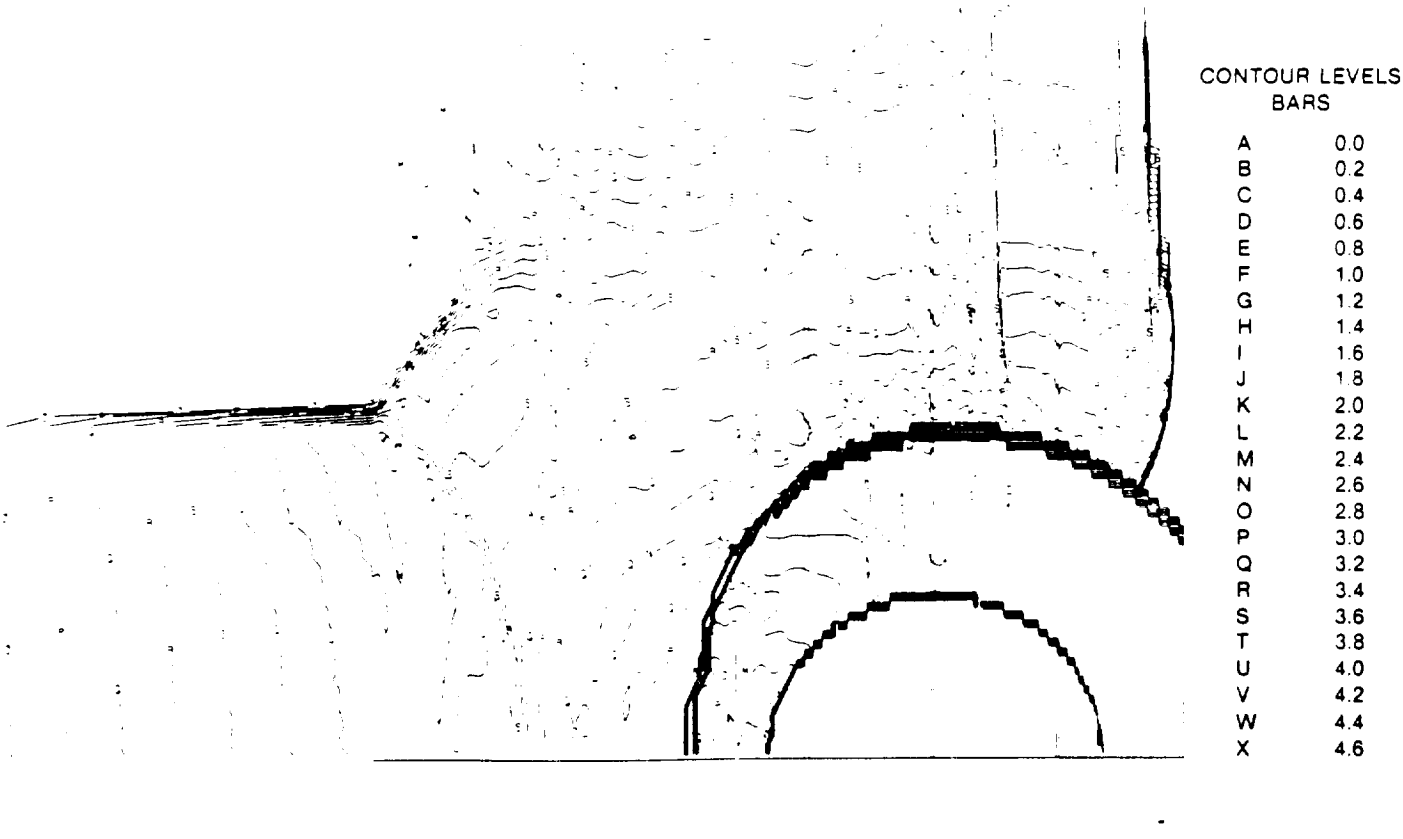

Figure 39. Pressure Contours Around Bay at 22.6 and 24.2 mSEC (Axis Normal To Flow Field)

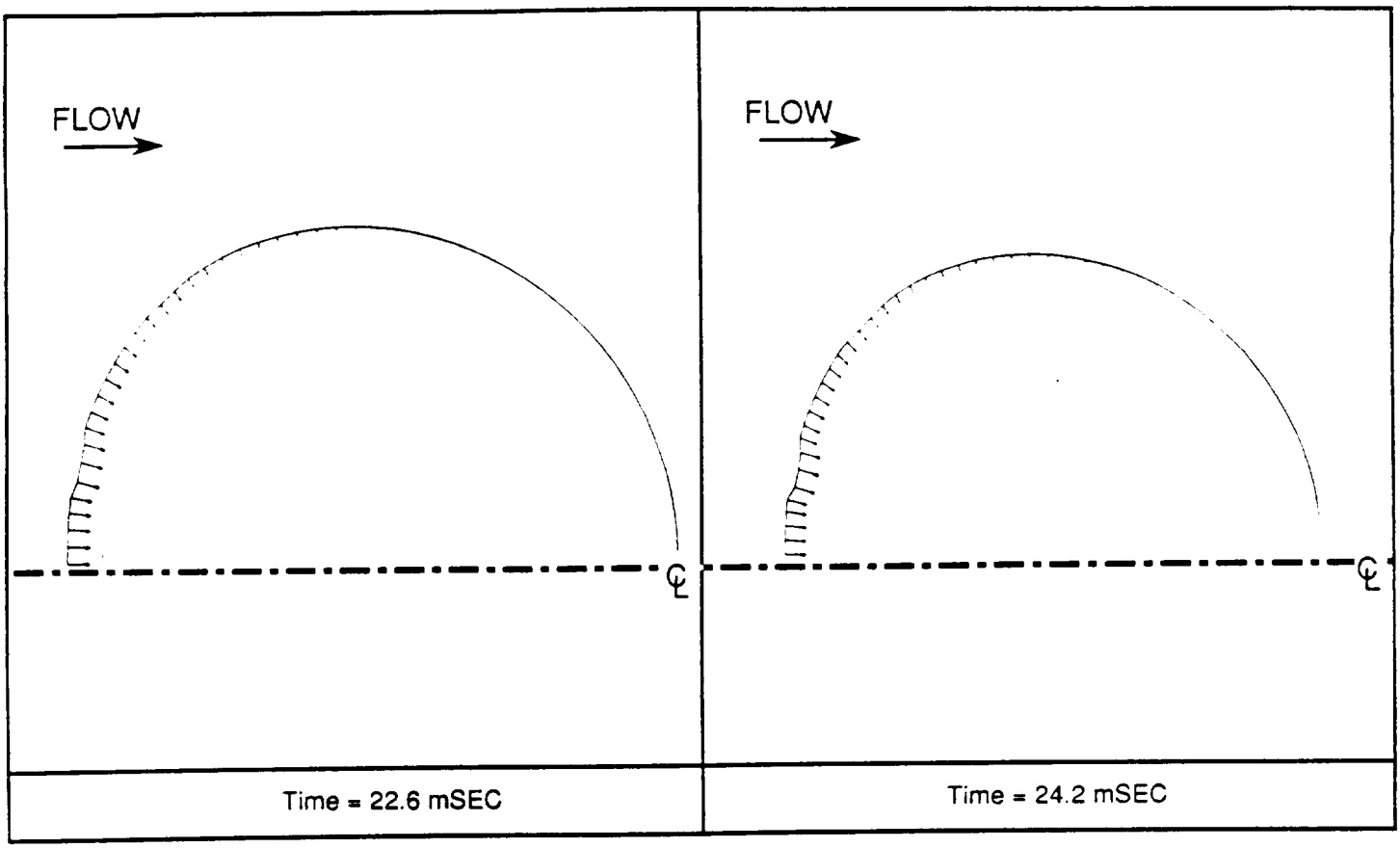

Figure 40. Velocity Vectors of the Imploding Cargo Bay at 22.6 and 24.2 mSEC

VII. RESPONSE OF RTG TO IMPACT OF FORWARD CLOSURE TITAN FRAGMENTS

The material presented in this section describes the analyses performed by FSC personnel to determine the response of the GPHS-RTG to the end-on impact of fragments from the forward SRM closure for the Titan-34D.

A. Model Description

A very detailed model of the RTG stack was set up in translational symmetry. The geometry of a typical RTG stack is shown in Figure 41. The stack contains two GPHS modules having detailed zoning. The aeroshells were modelled using the Lagrangian processor and an empirically developed equation of state for 3D-graphite. The four GIS (graphite impact shells) were modelled using the Lagrangian processor and 3D-graphite material with an OD of 1.550" and an a thickness of .217". The 0.025" thick iridium shells encapsulating the fuel pellets were modelled using the shell processor embedded in the PISCES code. The four fueled clads containing PuO_2 had an outer diameter of 2.744 cm and were modelled using the Lagrangian processor.

The two modules with the detailed zoning were placed in the 1 and 2 positions of the stack. In position 3, a detailed model of the aeroshell surrounds mass concentration for the fuel, iridium and graphite impact shell. The remainder of the stack was simulated with distributed mass blocks having the mechanical properties of poco graphite. The RTG housing was modelled as an aluminum shell of thickness 0.06" using the shell processor. The results of experiments conducted by GE to assess the compressive strength of the multifoil insulation package were transmitted to FSC. An equation of state for the foil package was derived by FSC personnel after taken into account the presence of the thermoelectric elements in the foil.

The titanium spider was simulated using the Lagrangian processor and the 0.57 inch graphite plate or thickness was modeled at the bottom of the stack. The mechanical properties of all the materials used are presented in Table V. The forward closure thickness of the SRM for the Titan 34D-7 was found to vary between 0.25" and 0.375".

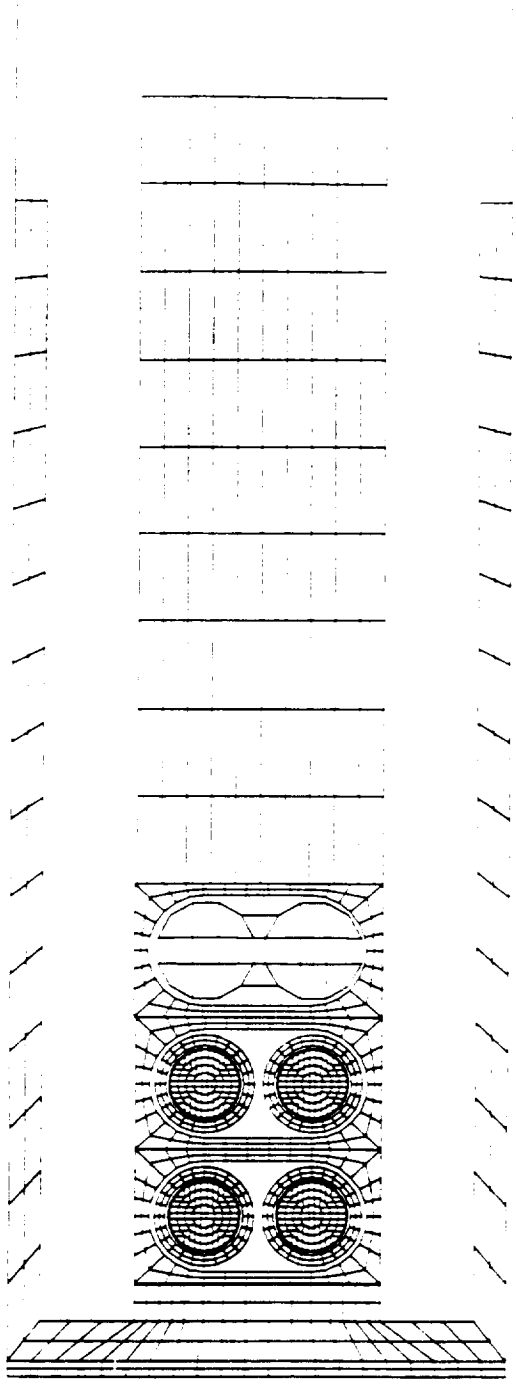

Figure 41. Detailed Geometry of RTG Stack

Table V. Summary Of Material Properties Used In The SRM Fragment Impact Analyses

MATERIAL	EQUATION OF STATE						YIELD MODEL				DATA SOURCE
	TYPE	(1)	BULK MODULUS KBAR	Y1 KBAR	Y2 KBAR	REF. DENSITY (o) gm/cc	TYPE	SHEAR MODULUS KBAR	YIELD STRENGTH KBAR	SPALL STRENGTH KBAR	
WEAK PLUTONIA (PU2H6H)	P-	0.84	730.	0.677	1.33	11.5	VON MISES	270.	0.677	0.200	LOS ALAMOS DATA SHEETS
STRONG PLUTONIA (PU4H13H)	P-	0.84	730.	1.30	1.33	11.5	VON MISES	270.	1.30	0.400	MAY 1986
WEAK URANIA (U6H11H)	P-	0.87	1370.	1.10	1.22	11.0	VON MISES	598.	1.10	0.600	LOS ALAMOS DATA SHEETS
STRONG URANIA (U8H12H)	P-	0.87	1370.	1.20	1.22	11.0	VON MISES	598.	1.20	0.800	MAY 1986
POCO GRAPHITE	POLY-NOMIAL	-	301.			1.98	VON MISES	20.	0.50	1.0	W.W. TARBELL (1979)
3-D GRAPHITE	SHOCK	-	25.9			1.95	VON MISES	20.	1.00	1.0	AFWL TR-79-38
IRIDIUM	POLY-NOMIAL	-	3510.			22.5	VON MISES	1618.	2.00	1000.	ORNL-5611 APRIL 1980 (3) FSAR GESP 7200 AUGUST 1985
INSULATION-T/E	P-	0.59	8.9			0.90	VON MISES	6.7	1.00	0.1	GE MEMO (2) C.J. EARDLEY 1/7/88
ALUMINIUM	POLY-NOMIAL	-	765.			2.77	VON MISES	294.0	6.50	1000.	BAKKEN & ANDERSON, SANDIA
D6A STEEL	POLY-NOMIAL	-	1670.			7.86	VON MISES	816.0	12.9	1000.	LADISH DATA SHEET FSCM # 07703 (1987)

(1) = $\frac{\text{DENSITY OF UNCOMPACTED MATERIAL}}{\text{DENSITY OF COMPACTED MATERIAL}}$

(2) DERIVED FROM EXPERIMENTS CONDUCTED AT GE AND MODIFIED BY FSC PERSONNEL TO ACCOUNT FOR THERMOELECTRIC ELEMENT INITIAL COMPRESSIVE STRENGTH

(3) YIELD CORRECTED FOR THE BIAXIAL TENSION CREATED BY THE ALMOST SPHERICAL NATURE OF THE IRIDIUM SHELL

S 074 58 05 89

A large number of parametric runs were made with the SRM fragment oriented face on impacting the RTG stack end-on. The thickness of the fragment was varied from 0.25" to 0.375". Impact velocities of 45, 120, and 228 m/s were assumed to span the range of the fragment velocities predicted for the Titan 34D.

Figure 42 exhibits the results of a typical calculation. A 1/4" thick steel fragment oriented face-on impacts the RTG stack end-on at 228 m/s. The four fuel capsules in position 1 and 2 of the stack are also shown.

Figure 43 shows a comparison of the response of the RTG stack when impacted at 45, 120, and 228 m/s by a 3/8" steel fragment. The ellipticities of the fuel capsules were calculated as a function of time and the maximum values are reported in Table VI. For the sake of comparison, an additional run was made with an SRB fragment (1/2") thick impacting the stack at 100 m/s. The deviation of the capsule from the initial circular shape is a measure of the insult suffered by the RTG.

Another series of runs were made with the fragment oriented edge-on to the RTG stack. Two different positions of the edge-on fragment were analyzed. First, the fragment was aligned with the centre of the stack and secondly, the fragment was aligned with the centre of one column of fuel capsules. The impact velocities studied were 100, 150, and 200 m/s. The fragment thicknesses analyzed were 0.25", 0.375", and 0.50".

Figure 44 exemplifies the results of the series of calculations performed with varying fragment thicknesses and alignments. For an impact velocity of 150 m/s, the fragment, aligned with the center of the stack does the most damage. When the impacting fragment is aligned with the center of the column of fueled capsules, the column of impacted capsules is badly damaged, although the capsules in the other column are left almost intact. Additionally, the thicker fragment impacts cause more damage than the thinner fragment. The ellipticities of the fuel capsules when the fragment is aligned with the center of the RTG stack are displayed in Table VII.

Table VIII displays the ellipticities calculated when the fragment is aligned with the center of the fueled capsules.

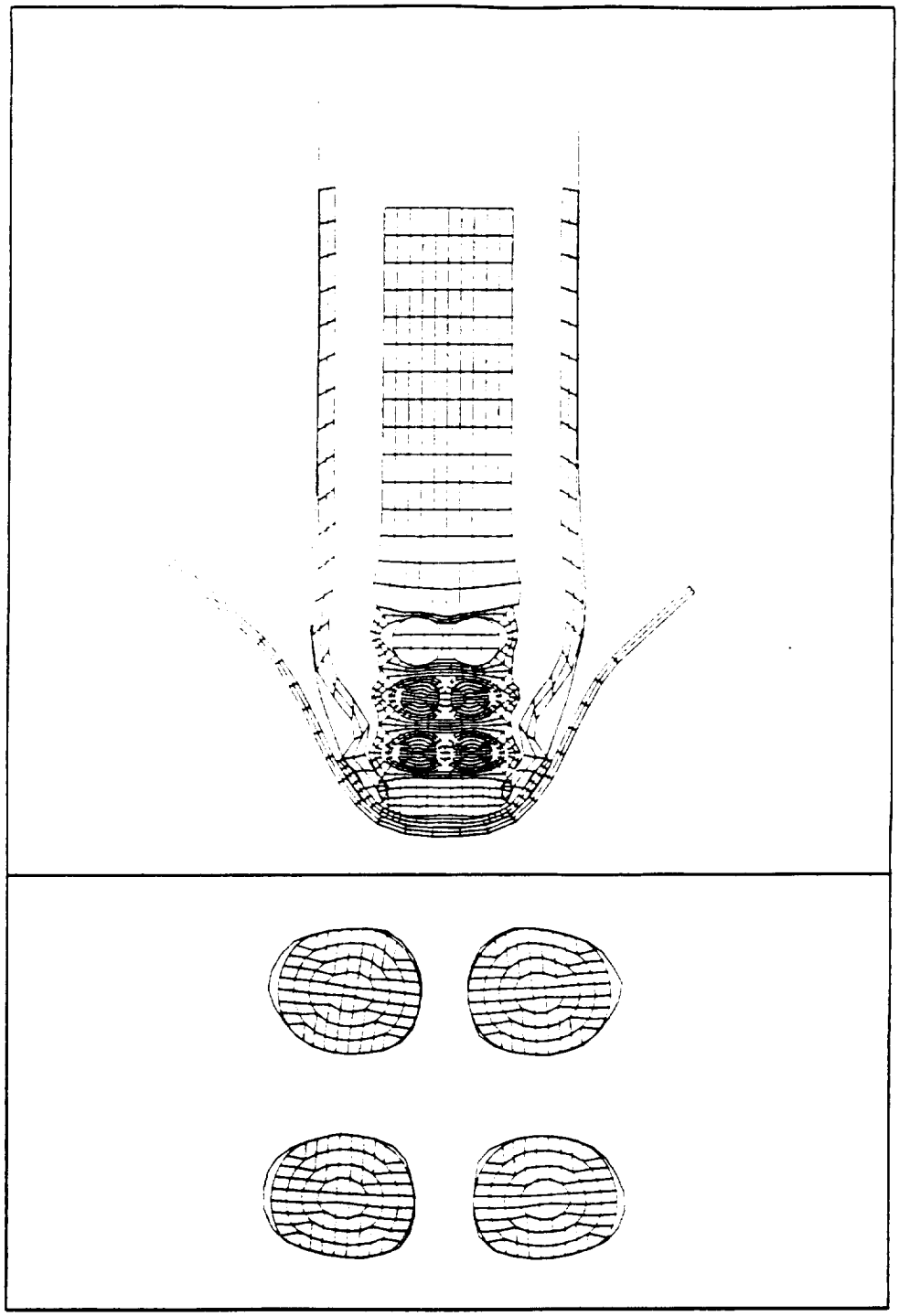

Figure 42. Response of RTG Stack Due to Impact of a 1/4″ Fragment at 228 m/s

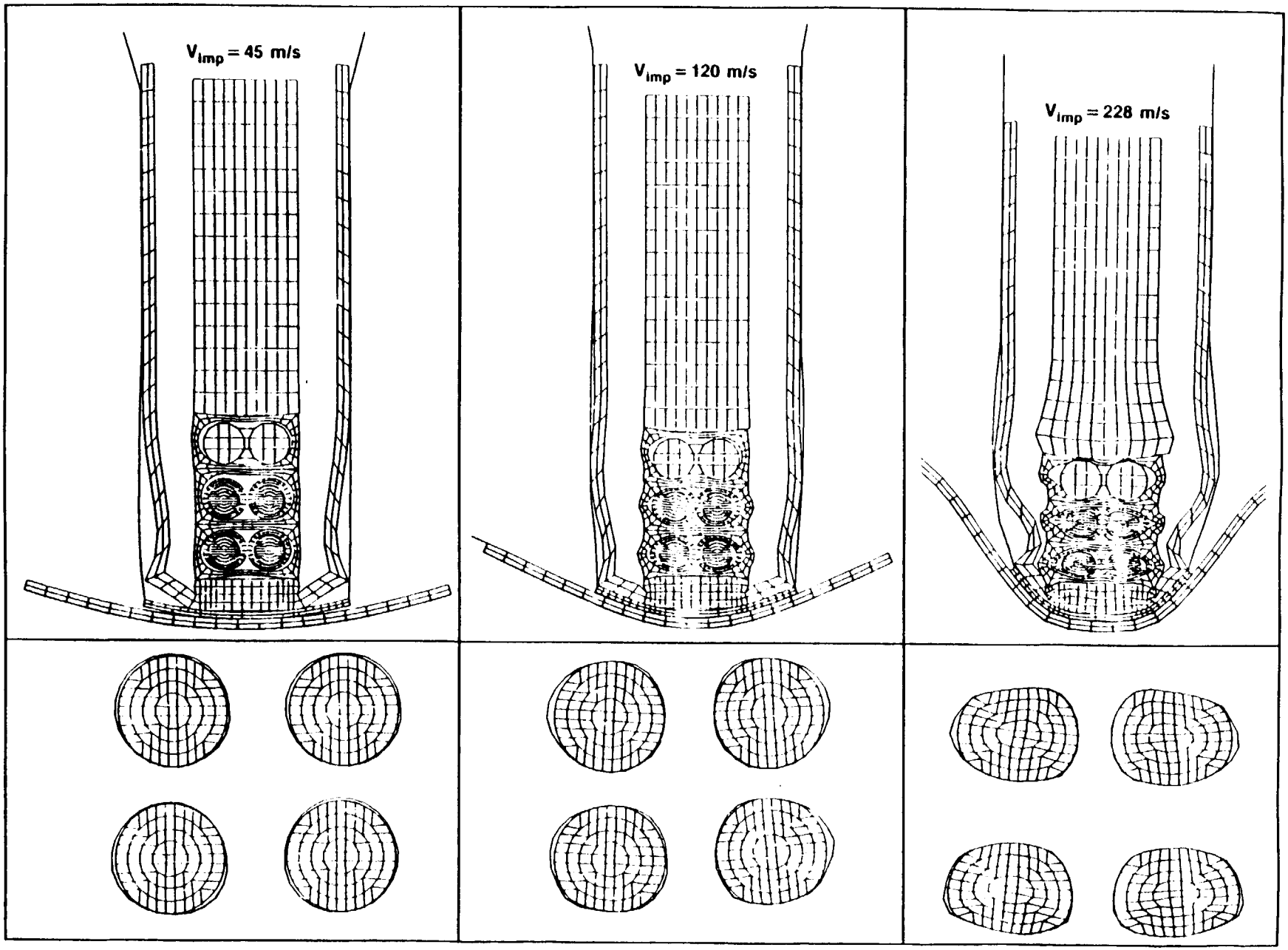

Figure 43. Comparison of RTG Response Due to Impact by a 3/8" Steel Fragment at 45 m/s, 120 m/s, and 228 m/s

Table VI. Summary of RTG Response to Titan SRM Dome Fragment Impacts at Various Velocities

Data Set Name [1]	Fragment Thickness	Fragment Size	Fragment Velocity	Position 1 Capsule Distortion	Position 2 Capsule Distortion
	INS	INS	M/S		
WP_P375_45	0.375	28X28	45	2.	0.
WP_P375_120	0.375	28X28	120	6.2	2.9
WP_P375_228	0.375	28X28	228	40.	33.
WP_P25_228	0.25	28X28	228	18.	13.
12_WP_EOSP_100	0.5	56X56	100	18.	18.

[1] The notation "WP" indicates the weak plutonium properties defined in the March 30, 1988 briefing at Gaithersburg [6].

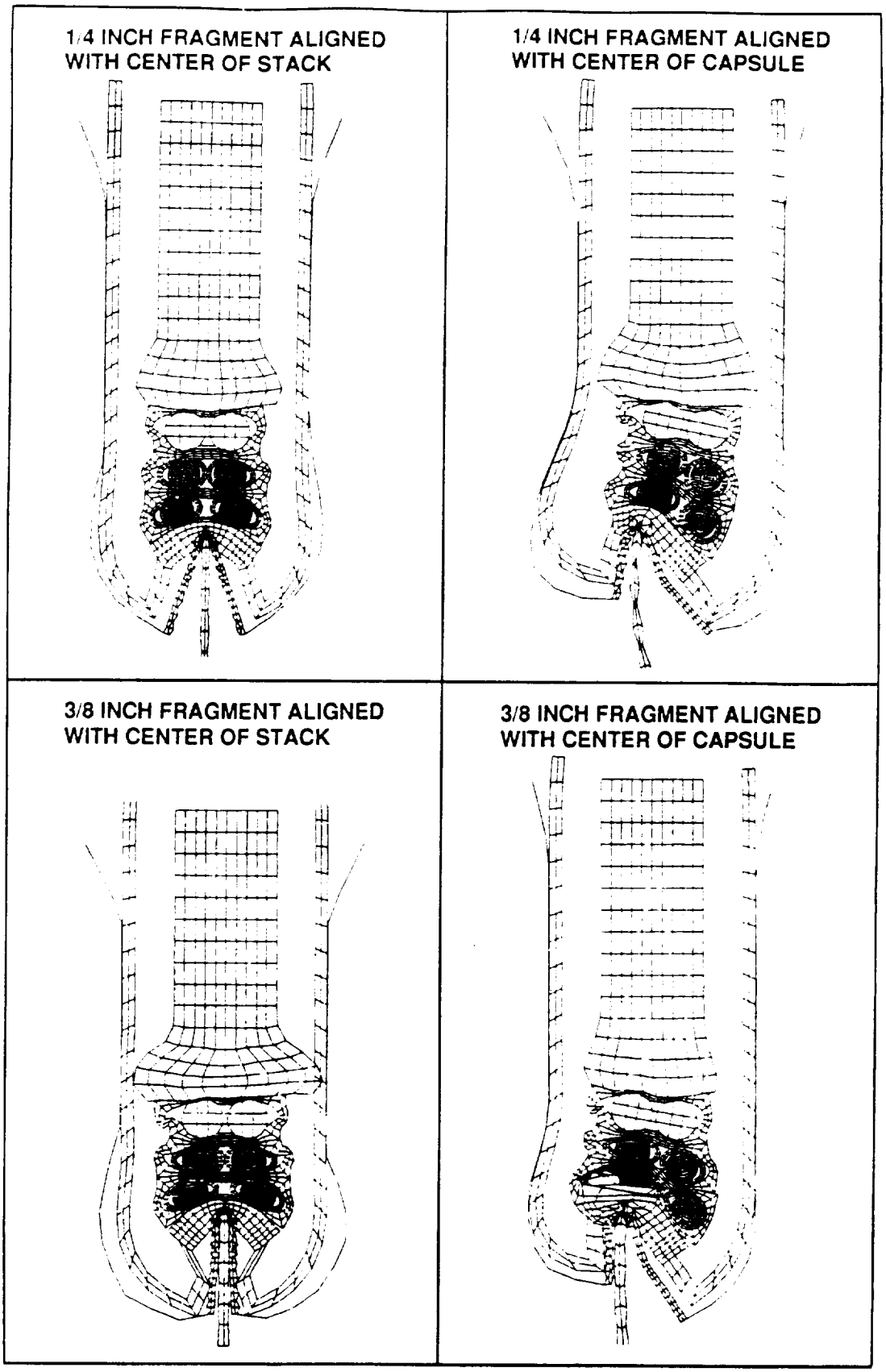

Figure 44. Comparison of RTG Response with Alignment and Thickness of Fragment Impacting at 150 m/s

Table VII. Distortion of Fueled Capsule with Fragment Aligned with Center of RTG Stack

	Edge-On Fragment		Capsule Ellipticities Fragment Aligned with Center of RTG Stack			
			Position 1		Position 2	
Data Set Name	Thickness in	Impact Velocity m/s	Capsule 1	Capsule 2	Capsule 1	Capsule 2
WP_P5_MID_150	1/2	150	93.9	93.9	63.5	63.5
WP_P5_MID_100	1/2	100	3.75	37.5	25.4	25.4
WP_P375_MID_150	3/8	150	70.0	70.0	54.7	54.7
WP_P375_MD_100	3/8	100	27.1	27.1	18.9	18.9
WP_P25_MID_150	1/4	150	55.8	55.8	33.3	33.3
WP_P25_MID_100	1/4	100	14.5	14.5	9.4	9.4

Table VIII. Distortion of Fueled Capsule with Fragment Aligned with Center of Capsule 1

	Edge-On Fragment		Capsule Ellipticities Fragment Aligned with Center of Capsule 1			
			Position 1		Position 2	
Data Set Name	Thickness in	Impact Velocity m/s	Capsule 1	Capsule 2	Capsule 1	Capsule 2
WP_P5_ED_100	1/2	100	43.6	12.5	35.1	-
WP_P5_ED_150	1/2	150	139.3	19.4	81.6	10.8
WP_P5_ED_200	1/2	200	>200	25.0	>200	14.1
WP_P375_ED_100	3/8	100	37.5	7.7	27.1	-
WP_P375_ED_150	3/8	150	91.4	12.5	61.5	7.7
WP_P375_ED_200	3/8	200	>200	19.1	131.8	10.7
WP_P25_ED_100	1/4	100	16.9	4.5	16.9	-
WP_P25_ED_150	1/4	150	71.4	7.5	43.6	2.9
WP_P25_ED_200	1/4	200	174.4	15.1	57.7	2.9

References

[1] Reynolds, Joel R, et al., "Final Report of the NASA/DOE/INSRP STS51L and Titan 34D-9 Explosion Working Group", June 16, 1989, NASA/Johnson Space Flight Center, Houston, TX.

[2] Mathews, F.H. Memo to Stan Bronisz. March 17, 1983. Sandia National Laboratories, Albuquerque, New Mexico.

[3] Lee E.L. et al., "Adiabatic Expansions of High Explosive Detonation Products" UCRL-50422, May 1968, Lawrence Livermore Laboratory, Livermore, California.

[4] Shapiro, A.H., The Dynamics and Thermodynamics of Compressible Fluid Flow, Ronald Press Co., NY, 1953-54.

[5] Baker, W.E., Explosions in Air, University of Texas Press, Austin, TX, 1973.

[6] Cull, T.A., T.G. George, D. Pavone. "General Purpose Heat Source Development: Safety Verification Test Program Explosion Overpressure Test Series," Los Alamos National Laboratory document LA-10697-MS, 9/1986.

[7] Eck, Marshall and Meera Mukunda. "On the Response of the GPHS Fueled Clad to Various Impact Environments," Fairchild report FSC-ESD-217/88/427, 1988.

[8] Bakken, L.H. and Anderson, P.D. The Complete Equation of State Handbook, 1967.

[9] Herrman W. Constitutive Equations for the Dynamic Compaction of Ductile Porous Materials. J. Appl. Phys 40 2490-2499, 1966.

[10] Lehto, D.L. "Blast From a Cylindrical Centaur Propellant Explosion." Naval Surface Warfare Center (NSWC), Silver Spring, MD, 1985.

[11] Chemical Engineer's Handbook, 4th ed. McGraw Hill, NY, 1963, pages 3-195.

[12] McCarty, R.D. "Hydrogen Technological Survey-Thermophysical Properties", NASA SP-3089, 1975.

[13] Woolley, H.W., R.B. Scott, and F.G. Brickwedde, "Compilation of Thermal Properties of Hydrogen in its Various Isotopic and Ortho-Para Modifications," Journal of Research of the National Bureau of Standards, Research Paper RP 1932, Volume 41.

[14] Marsh, S.P., LASL Shock Hugoniot Data, University of California Press, 1980, page 85.

[15] Nellis, W.J., M. Ross, M. van Thiel, A.C. Mitchell, and G.J. Devine, "The Shock Compression of Liquid H2 to 10 GPa (100 kbar)," Shock Waves in Condensed Matter, American Institute of Physics Conf. Proceedings No. 78, 1981, pages 223-225.

[16] Fickett, W. and W.C. Davis, Detonation, University of California Press, 1979, pages 133-162.